Discover Oncology

Research

Novel marker genes and small molecule drugs for radiotherapy resistance in cervical cancer identified based on single-cell multi-omics analysis

Yang Liu[1] · Xin Pan[1] · Xu Zhang[1] · Bo Tan[1] · Rui Ran[1] · Li Liu[1] · Lin Yang[2] · Zhiliang Wang[1,3]

Received: 11 December 2024 / Accepted: 29 April 2025
Published online: 19 May 2025

Abstract
Radiotherapy is the cornerstone of treatment for cervical cancer, yet the variability of patient response demands a deeper understanding of the molecular determinants of radioresistance. In this study, we investigated the molecular and cellular mechanisms of radioresistance in cervical cancer through a comprehensive multi-omics and machine learning approach. We downloaded and processed transcriptome sequencing, methylation and single-cell sequencing data from the TCGA and GEO databases. Differential gene and methylation analyses were performed to identify radioresistance-related markers. Single-cell data were processed using Seurat and annotated using CellTypist. Prognostic models were constructed and validated through downscaling, cell scoring, trajectory analysis and machine learning. Additionally, immune infiltration and drug sensitivity analyses were conducted. The differential analysis identified 845 up-regulated and 460 down-regulated genes associated with radioresistance. The methylation analysis identified 3042 down-regulated and 158 up-regulated gene loci. Single-cell sequencing revealed 43,475 cells and 13 cell types, with aneuploid cells predominantly present in epithelial cells. Cell scoring highlighted dispersed immune cells, with monocytes, ILCs, and T cells being the most relevant to radiotherapy resistance. The machine learning approach constructed a robust prognostic model using Cox regression and validated it on multiple datasets. The prognostic model demonstrated good predictive ability in assessing radiotherapy efficacy and immune infiltration. Drug screening identified several potential therapeutic candidates with high sensitivity for high-risk patients. This study provides a comprehensive multi-omics analysis and machine learning framework for identifying and validating molecular markers and prognostic models associated with radioresistance in cervical cancer, providing insights for personalized treatment strategies.

1 Introduction

Cervical cancer is one of the common malignant tumours among women worldwide, with a high incidence especially in developing countries [1]. According to the statistics of the World Health Organization (WHO), there are more than 500,000 new cases of cervical cancer worldwide each year, and more than 85% of the cases occur in developing

Supplementary Information The online version contains supplementary material available at https://doi.org/10.1007/s12672-025-02532-0.

✉ Zhiliang Wang, docwang@hospital.cqmu.edu.cn | [1]Department of Obstetrics and Gynecology, The Second Affiliated Hospital, Chongqing Medical University, Chongqing 400010, China. [2]Department of Gynecology, The First Affiliated Hospital, Chongqing Medical University, Chongqing 400042, China. [3]Department of Obstetrics and Gynecology, Affiliated Hospital of Zunyi Medical University, Zunyi 563000, China.

countries [2]. In the GLOBACON 2022 global cancer statistics, cervical cancer ranks as the 8th most commonly diagnosed cancer [3]. High-risk human papillomavirus (HPV) infection is also a major cause of cervical cancer [4, 5]. In addition, other factors such as immune status, genetic susceptibility and environmental exposures may also be involved in the development and progression of cervical cancer.

In the treatment of cervical cancer, regardless of subtype and HPV infection status, the first-line therapy for patients typically includes surgery, radiotherapy, chemotherapy, or a combination of these treatments [6]. Currently, chemotherapy is used in cervical cancer patients as an adjunct to definitive local treatments (surgery or radiotherapy) to improve prognosis, as well as to provide palliative care for those with recurrent or newly diagnosed metastatic disease [7]. With the development of targeted therapies and biologics, the use of the anti-VEGF antibody bevacizumab has gained attention as a targeted treatment option [8]. Immunotherapy has also brought new hope for cervical cancer treatment, particularly by enhancing the host immune response against HPV-positive cancer cells through the combination of antigen-specific immunotherapeutic approaches, such as vaccines or adoptive cell transfer [9]. However, Radiotherapy is usually used as an important tool in the treatment of cervical cancer [10], especially in locally advanced cervical cancer, radiotherapy combined with concurrent chemotherapy (CCRT) is considered as a standard treatment option [11]. However, the efficacy of radiotherapy varies from patient to patient, and some patients develop resistance to radiotherapy, leading to treatment failure and disease progression; this resistance may stem from a variety of factors such as genetic and epigenetic variations in tumour cells, changes in the microenvironment, and immune escape [12]. Therefore, there is an urgent need for in-depth study of the molecular mechanisms of radiotherapy resistance and the search for new therapeutic targets to improve the efficacy of radiotherapy.

Single-cell sequencing technology has made significant progress in biomedical research in recent years, especially in tumour research, providing a powerful tool for revealing tumour heterogeneity and treatment resistance mechanisms [13]. Single-cell RNA sequencing (scRNA-seq) technology enables high-throughput analysis of gene expression profiles of individual cells, thereby identifying the characteristics of different cell populations in tumour tissues and revealing key genes and signaling pathways associated with radiation therapy resistance [14]. In particular, in cervical cancer research, the use of single-cell sequencing technology allows detailed analysis of various cell types and their gene expression profiles in tumour cells and microenvironments; one study identified several key genes and signalling pathways associated with radiotherapy resistance through scRNA-seq analysis of tumour samples before and after radiotherapy in cervical cancer patients [15]. To further validate the role of differential genes in radiotherapy resistance, the researchers combined large-scale transcriptomic data from the TCGA database and single-cell datasets from the GEO database for comprehensive analysis. For example, the expression of DNA damage repair genes such as BRCA1, BRCA2 and RAD51 was significantly upregulated in radiotherapy-resistant cells. The up-regulation of these genes may have enhanced the ability of tumour cells to repair radiation-damaged DNA, thereby improving cell survival. Cell cycle regulatory genes such as CDK4 and CDK6 were up-regulated in the expression of radiotherapy-resistant cells, and these genes promoted cell proliferation, thereby accelerating tumour growth and spread [16]. In addition, some differentially methylated sites associated with radiotherapy resistance were identified by differential methylation analysis. The methylation status of these loci may affect gene expression and thus play an important role in radiotherapy resistance. For example, the hypermethylation status of the MGMT gene is associated with radiotherapy resistance, while its hypomethylation status is associated with radiotherapy sensitivity [17]. By using a combination of single-cell sequencing technology and large-scale transcriptomic data, researchers not only identified key genes and signaling pathways associated with radiotherapy resistance, but also revealed changes in cell types and immune cells in the tumour microenvironment. These findings provide new perspectives for understanding the mechanisms of radiotherapy resistance in cervical cancer and lay the foundation for developing new therapeutic targets and strategies.

In this study, we systematically explored the molecular and cellular mechanisms of radiation therapy sensitivity in cervical cancer using multi-omics and machine learning approaches. Transcriptome sequencing, methylation data, and single-cell sequencing data from TCGA and GEO databases were downloaded and processed to identify markers associated with radiation therapy sensitivity through differential gene and methylation analysis. We also constructed and validated a robust prognostic model with good predictive ability across multiple datasets using machine learning methods. Furthermore, immune infiltration and drug sensitivity analyses were performed to screen potential therapeutic agents with high sensitivity for high-risk patients. This study establishes the foundation for personalized treatment of radiotherapy resistance in cervical cancer and provides potential targets for clinical intervention.

2 Methods

2.1 Bulk sequencing data, methylation data and clinical information downloads

We used TCGAbiolinks [18] to download The cancer genome atlas (TCGA, https://www.cancer.gov/ccg/research/genome-sequencing/tcga) database for all bulk sequencing data for cervical cancer and methylation sequencing data for the 450 K platform. At the same time, we obtained all the bulk sequencing data from UCSC Xena database (https://xena.ucsc.edu/) to download and collate the clinical phenotype data of cervical cancer.

2.2 Differential genes screening

To screen for differential genes associated with radioresistance, we matched the bulk sequencing data with clinical information, retaining only samples that had undergone radiotherapy and had a treatment outcome of Complete Response (CR) or Progressive Disease (PD), resulting in 112 Complete Response samples, 23 Progressive Disease samples. We considered patients treated with radiotherapy with a Progressive Disease outcome to be radioresistance and patients treated with radiotherapy with a Complete Response outcome to be radioresistance. We used the edgeR [19] package (version 4.0.2) to identify differential genes between groups, and genes satisfying P value < 0.05, logFC > 1 were considered as radiotherapy sensitivity-related differential genes.

2.3 Differential methylation genes screening

To screen for differentially methylated genes associated with radioresistance, we matched the methylation sequencing data with clinical information and retained only samples that had undergone radiotherapy and had a treatment outcome of Complete Response (CR) or Progressive Disease (PD), resulting in 112 Complete Response samples and 23 Progressive Disease samples. Finally, 112 Complete Response samples and 23 Progressive Disease samples were obtained. In order to obtain radiotherapy susceptibility-related differentially methylated genes with high confidence, we normalised the methylation matrix using the champ.norm function in the CHAMP (2.32.0) package[20], and then filtered the differentially methylated loci using the champ.DMP function.

The specific screening and workflow can be found in Table 1.

2.4 Single-cell sequencing data download and pre-processing

We processed single-cell data using the Seurat (version 4.4.0) R package [21], downloaded the cervical cell expression profiling dataset GSE168652 [22] GSE208653 [23] from the GEO (https://www.ncbi.nlm.nih.gov/geo/) database with a reliable source of samples, and the sequencing platform was based on the GPL24676 Illumina NovaSeq 6000 (Homo sapiens). We obtained three cervical cancer samples and two normal cervical samples from the GSE168652 dataset, and one cervical cancer sample and one normal cervical sample from the GSE208653 dataset. One sample of cervical cancer and one sample of normal cervix were obtained from the GSE208653 data set. The single-cell data were filtered by setting each gene to be expressed in at least 3 cells and each cell to express at least 250 genes, and the PercentageFeatureSet function was used to calculate the percentage of mitochondrial, ribosomal and erythrocyte genes, and to ensure that the genes expressed in each cell were greater than 500 and less than 4000, and the UMI of each cell was less than 5000, and the mitochondrial genes were less than 5000. The PercentageFeatureSet function calculates the percentage of

Table 1 PRISMA analysis workflow

Item	Type of analysis	R package	Key parameters
Differential analysis	Differential genes screening	edgeR	$P < 0.05$, $\|logFC\| > 1$
	Differential methylation genes screening	CHAMP4	$P < 0.05$, $\|logFC\| > 0.1$
Functional annotation	Gene ontology	clusterProfiler	Benjamini–Hochberg correction, $P < 0.05$
	Kyoto Encyclopedia of Genes and Genomes	clusterProfiler	Benjamini–Hochberg correction, $P < 0.05$

mitochondrial and ribosomal genes and ensures that each cell expresses more than 500 genes and less than 4000 genes, and each cell has a UMI of less than 5000.

From the GSE168652 dataset, we obtained three cervical cancer samples and two normal cervical samples, while from the GSE208653 dataset, we acquired one cervical cancer sample and one normal cervical sample. After merging the raw data, we first checked the metadata for each sample, confirming a total cell count of 70,280 (before filtering). After quality control, the filtered data contained 43,475 cells. Next, we used the NormalizeData function to normalize the data, employed FindVariableFeatures to identify highly variable genes, and performed data scaling using ScaleData. Subsequently, we conducted principal component analysis (PCA) using RunPCA, selecting 50 principal components, and then applied the Harmony algorithm (with Sample as the grouping variable) to correct for batch effects, alleviating technical differences between different batches.

Regarding cell type annotation, in addition to initial cell clustering based on clustering results, we integrated the majority voting results provided by the Celltypist tool and incorporated copy number variation information obtained from CopyKat analysis. Specifically, for cells originally labeled as"Epithelial cells"that were identified as"aneuploid"in the CopyKat results, we reclassified them as"Aneuploid."

2.5 Downscaling and annotation

We standardized the sample data separately by log-normalization. Highly variable genes were searched for by the FindVariableFeatures function (identifying variable features based on variance stabilisation transformations ("vst")), followed by scaling by using the ScaleData function for all genes, and in order to avoid the batch effect of the samples the Harmony package (version 0.1.0) [24] was used to batch correct the samples. We performed cell type annotation via the Immune_All_High model from CellTypist [25]. At the same time, we used the tool copykat (version 1.0.8) [26] to identify aneuploid cells, and then filtered the marker genes of each subpopulation by the FindAllMarkers function with the thresholds of |logFC|> 0.5, minpct > 0.5, and p_val_adj < 0.05. Single-cell subpopulation differential gene enrichment was performed using the FeatureHeatmap function in the SCP package (version 0.5.2)[27].

2.6 Cell scoring

To further explore the expression of radiotherapy resistance related genes at the cellular level, we first took the intersection of genes involved in differential genes and differential methylation sites, and based on these intersected genes we scored the cells using the AUCell (1.22.0) package [28], and identified high scoring cells using the AUCell_exploreThresholds function. To further understand the function of these cells, we used the FindMarkers function to identify differences between high and low scoring groups.

2.7 Trajectory analysis of aneuploid malignant cells

We first performed an initial downward clustering based on the aneuploid cells predicted by kopykat, observing the AUCell scores among the clustered subgroups. The trajectory analysis of aneuploid cells was then performed using the RunMonocle2 function of the SCP package, and to determine the developmental starting point, we used the CytoTRACE (version 0.3.3) package [29] for prediction of cell differentiation potential.

2.8 Machine learning to construct prognostic models

We performed one-way Cox regression analyses of the genes involved in the intersection of differential genes and differentially methylated loci on samples with a survival time greater than 30 days (273 cases), and divided the data into training and validation sets at a 7:3 ratio. To address multicollinearity in the variables, Lasso regression analyses were performed on the training set using the glmnet package (version 4.1-4) [30]. To build a robust prognostic model, we use survival (version 3.5–7) [31], CoxBoost (version 1.5) [32], gbm (version 2.1.8.1) [33], randomForestSRC (version 2.1.8.1) packages [34] on the training set based on the genes screened by the Lasso algorithm. The Cox algorithm was implemented using default parameters in the survival package. For the CoxBoost algorithm, the penalty parameter was tuned via optimCoxBoostPenalty (start.penalty = 500, maxstepno = 200, minstepno = 50, iter.max = 10), and the optimal step number was determined by cv.CoxBoost using tenfold cross-validation (K = 10, type ="verweij", maxstepno = 500, penalty = optimized value). The final model used stepsize.factor = 1, sigmoid standardization, and standardized covariates. The

GBM algorithm was trained with the optimal number of trees (n.trees = best), interaction.depth = 3, n.minobsinnode = 10, shrinkage = 0.001, and tenfold cross-validation (cv.folds = 10). The Random Survival Forest (RSF) was built using rfsrc with ntree = 500 trees, mtry = sqrt(p) for splitting variables, nodesize = 15 (survival default), splitrule ="logrank", and bootstrap ="by.root", while variable importance and proximity matrices were disabled (importance ="none", proximity = FALSE). Model validation was performed on the validation set, and the best-performing algorithm was selected by comparing the AUC values and median survival of the models at 1, 3, and 5 years to establish our radiotherapy sensitivity-related prognostic model.

2.9 Comparison of models with clinical variables

To further assess the significance of our model, we compared the model to the clinical information. We first scored the sample according to the model, divided the sample into high- and low-risk groups according to the median score, and then used chi-square tests to compare the high- and low-risk groups with the clinical information. To determine that our model was an independent prognostic factor, we used univariate Cox and multivariate Cox for OS (Overall Survival: Overall Survival), DSS (Disease Specific Survival: Disease Free Survival), DFI (Disease Free Interval: Disease Free Interval), PFI (Progression Free Interval), and PFI (Progression Free Interval: Disease Free Interval), respectively. and PFI (Progression Free Interval: Progression Free Interval) levels.

2.10 Immune infiltration

To further understand the model and tissue immune cell infiltration, we used the IOBR (version 0.99.9) package [35] to compute the immune infiltration obtained by seven immune infiltration assessment algorithms: MCPcounter, EPIC, xCell, CIBERSORT, QUANTIseq, ESTIMATE, and TIMER, and visualised them to a heat map is used to describe the immune landscape between subtypes. We also used the spearman algorithm to calculate the level of correlation between the immune infiltration scores assessed by the different algorithms and the model scores and genes within the model, which were also visualised on a heat map for comparison.

2.11 Drug screening

Expression profiling data and somatic mutation data for human cancer cell lines (CCLs) were obtained from the Broad Institute-Cancer Cell Line Encyclopedia (CCLE) project (https://portals.broadinstitute.org/ccle/) [36]. CERES scores for genome-scale CRISPR knockdown screening of 18,333 genes in 739 cell lines were obtained through the DepMap portal (https://depmap.org/portal/). CERES scores are used to measure the dependence of a gene of interest on a specific CCL, with lower scores indicating that the gene has been detected in the cellular growth and survival of a specific CCL. CERES scores are used to measure the dependence of the gene of interest on a particular CCL, with lower scores indicating that the gene is more essential for cell growth and survival in a particular CCL.

Drug sensitivity data for CCLs were obtained from the Cancer Treatment Response Portal (CTRP v.2.0, released in October of the year 2015, https://portals.broadinstitute.org/ctrp) and the PRISM repurposed dataset (19Q4, released in December of the year 2019, https://depmap.org/portal/prism/).CTRP contains sensitivity data for 481 compounds on 835 CCLs, while PRISM contains sensitivity data for 1448 compounds on 482 CCLs. Both datasets use area under the curve (AUC) values as a measure of drug sensitivity, with lower AUC values indicating increased sensitivity to treatment. Missing AUC values were filled in using k-nearest neighbour (k-NN) interpolation. Compounds with more than 20% missing data were excluded prior to interpolation. As the CCLs in both datasets were from the CCLE project, the molecular data from CCLE were used for subsequent CTRP and PRISM analyses.

Using the pRRophetic (version 0.5) software package [37] with built-in ridge regression modelling, the drug response of the clinical samples was predicted based on the purified expression profiles of the clinical samples to obtain an estimate of the AUC value for each compound in each clinical sample. Two different approaches were then used to identify drug candidates with high drug sensitivity in patients with high-risk scores. First, differential drug response analyses were performed in the high risk (top quartile) and low PPS (bottom quartile) groups to identify compounds with lower estimated AUC values in the high-risk group than in the low risk group. Second, Spearman's correlation analysis of AUC values with RiskScore scores was used to screen for compounds with the three largest negative correlations [38].

2.12 Enrichment analysis

The above batch differential gene analysis, differential methylation analysis, Gene ontology (GO) and Kyoto Encyclopedia of Genes and Genomes (KEGG) enrichment analysis of the results of the single-cell high- and low-scoring intergroup analysis were performed by clusterProfiler (version 4.10.0) [39], where the single-cell enrichment analysis was visualized by aPEAR (34) (version 1.0.0). The clusterProfiler (version 4.10.0) was used to perform the enrichment analyses, and the single-cell enrichment analyses were visualized by aPEAR (version 1.0.0) [40].

2.13 Specimen collection

Fresh cervical cancer (CC) tissues were meticulously collected from patients undergoing radiotherapy at The Second Affiliated Hospital, Chongqing Medical University. The diagnosis and classification of cervical cancer were performed by experienced pathologists to ensure the accuracy of disease characterization. The study protocol received approval from the Ethics Committee of the Second Affiliated Hospital, Chongqing Medical University (Approval No. 216). To maintain the integrity of the specimens, the tissues were collected before the initiation of radiotherapy and were not influenced by any prior treatment, ensuring that the samples accurately reflect the untreated tumor biology.

2.14 qPCR experiments

Total RNA was extracted from the collected tissue samples using the RNA-easy Isolation Reagent (No. RC112-01, Vazyme, China). Subsequently, quantitative real-time PCR (qRT-PCR) was performed to assess the expression levels of SCUBE1, JAKMIP1, LRRN4, KCNJ6, and RGS6. The cDNA synthesis was conducted using the HiScript III 1 st Strand cDNA Synthesis Kit (No. R312-01, Vazyme, China), followed by amplification with the ChamQ™ Universal SYBR®qPCR Master Mix (No. Q712-02, Vazyme, China), adhering strictly to the manufacturer's protocols.

2.15 Immunohistochemistry experiments

Immunohistochemical analysis was performed on paraffin-embedded tissue sections to evaluate the protein expression of SCUBE1, JAKMIP1, LRRN4, KCNJ6, and RGS6. The tissue sections were first deparaffinized, rehydrated, and subjected to antigen retrieval procedures. Following this, the sections were incubated overnight with primary antibodies specific to SCUBE1, JAKMIP1, LRRN4, KCNJ6, and RGS6, each at a dilution of 1:200. Detection of antibody binding was accomplished using a secondary streptavidin–horseradish peroxidase-conjugated antibody, with visualization via DAB substrate chromogen solution. Finally, the slides were counterstained with hematoxylin and cover slipped.

2.16 Clone formation experiments

To evaluate the clonogenic potential of the cells, a clone formation assay was performed. Cells were seeded at a density of 1×10^3 cells per well in 6-well plates, ensuring even distribution. The cells were cultured for 7 days in a complete medium containing 10% fetal bovine serum (FBS), under standard incubation conditions. The formation of colonies was assessed by staining the plates with crystal violet.

2.17 Transwell experiments

Transwell migration and invasion assays were conducted to assess the motility and invasive properties of the cells. For migration assays, 1.5×10^5 cells were resuspended in 200 µl of serum-free DMEM and placed in the upper chamber of a Transwell insert (Corning, NY, USA). The lower chamber was filled with 700 µl of DMEM supplemented with 20% FBS to serve as a chemoattractant. After a 24-h incubation at 37 °C, non-migrated cells on the upper side of the membrane were carefully removed, and migrated cells were fixed with methanol and stained with 0.5% crystal violet. For invasion assays, a similar procedure was followed, with the addition of a Matrigel coating on the Transwell membrane to simulate the extracellular matrix. After appropriate incubation times, the stained cells were imaged and quantified using an Olympus microscope (Tokyo, Japan), with results analyzed for cell migration and invasion efficiency.

2.18 Statistical analysis

All statistical analyses were performed using R software 3.5.3 and GraphPad Prism v. 8.01 (GraphPad Software, La Jolla, CA, USA). Student's *t* test was used to compare values between the test and control groups, and $P < 0.05$ was considered significant.

3 Results

3.1 Batch sequencing difference analysis

Through differential analysis, we identified 845 genes that were up-regulated in PD and 460 genes that were down-regulated in PD, among which the most significant up-regulated genes included DPEP3, ACTA1, PTGDR2, etc., and the most significant down-regulated genes included ALDH8 A1, BTNL8, CLDN2, etc. (Fig. 1A, B). For the GO enrichment analysis of the differential genes, the three most significant items enriched in the PB part were neuropeptide signaling pathway, keratinisation, and hormone metabolic process (Fig. 1C), and the three most significant items enriched in the CC part were external side of plasma membrane, monoatomous membrane and plasma membrane, and the three most significant items were external side of plasma membrane, monoatomous membrane and plasma membrane. plasma membrane, monoatomic ion channel complex, and postsynaptic membrane (Fig. 1D), and the three most significant

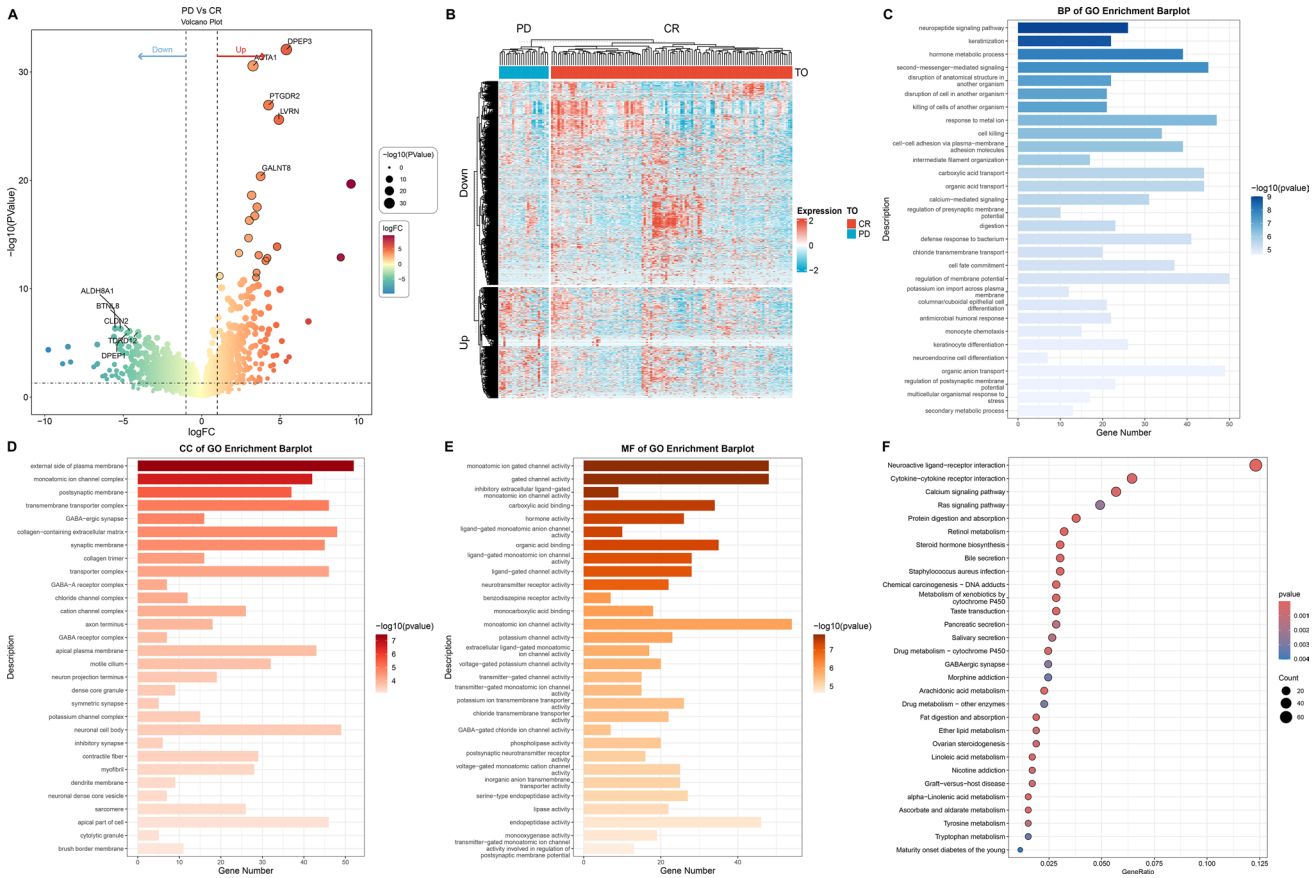

Fig. 1 Analysis of variance and enrichment between radiotherapy-sensitive and insensitive groups. **A** Difference-in-difference analysis volcano plot, PD vs CR, the redder the mark the greater the up-regulation, the bluer the mark the greater the degree of down-regulation. **B** Variance analysis heat map. **C** GO enrichment analysis The BP part enriched the most significant 30 articles, and the darker the colour, the more significant. **D** GO enrichment analysis of the 30 most significantly enriched lines in the CC fraction, the darker the colour, the more significant. **E** GO enrichment analysis The MF fraction enriched the 30 most significant articles, and the darker the colour, the more significant. **F** KEGG enrichment analysis of the 30 most significantly enriched entries

items enriched in the MF fraction were monoatomic ion gated, channel activity, gated channel activity, inhibitory extracellular ligand-gated monoatomic ion channel activity (Fig. 1E). We also observed a number of important pathways in KEGG-enriched results, such as Neuroactive ligand-receptor interaction, Cytokine-cytokine receptor interaction, Calcium signaling pathway, Ras signaling pathway (Fig. 1F). signaling pathway (Fig. 1F).

3.2 Methylation sequencing differential analysis

We screened a total of 3042 methylation sites downregulated in PD and 158 methylation sites upregulated in PD by differential analysis. After correlation screening, 1832 genes were involved, among which the most significantly up-regulated ones included cg00676711, cg05810129, cg20157314, etc., and the most significantly down-regulated ones included cg26159990, cg08297640, cg02988764, etc. (Fig. 2A, B). For the GO enrichment analysis of genes involved in differentially methylated loci, the most significant three items enriched in the BP part were forebrain development, axonogenesis, and neuron projection guidance (Fig. 2C), and the most significant three items enriched in the CC part were neuron to neuron synapse, asymmetric synthetic synapse, and so on (Fig. 2C). synapse, asymmetric synapse, neuronal cell body (Fig. 2D), and in the MF section, the three most significant enriched entries were potassium channel activity, potassium ion transmembrane transporter activity, monoatomic cation channel activity, and neuron projection guidance (Fig. 2C). activity, monoatomic cation channel activity (Fig. 2E). KEGG enrichment analysis of these genes significantly enriched many critical pathways in tumours, such as: cAMP signaling pathway: cAMP signaling pathway plays an important role in many cellular processes, including cell proliferation, apoptosis, and DNA damage repair, etc.; calcium signaling pathway: calcium signaling pathway is involved in many cellular processes, such as cell proliferation, apoptosis, and DNA

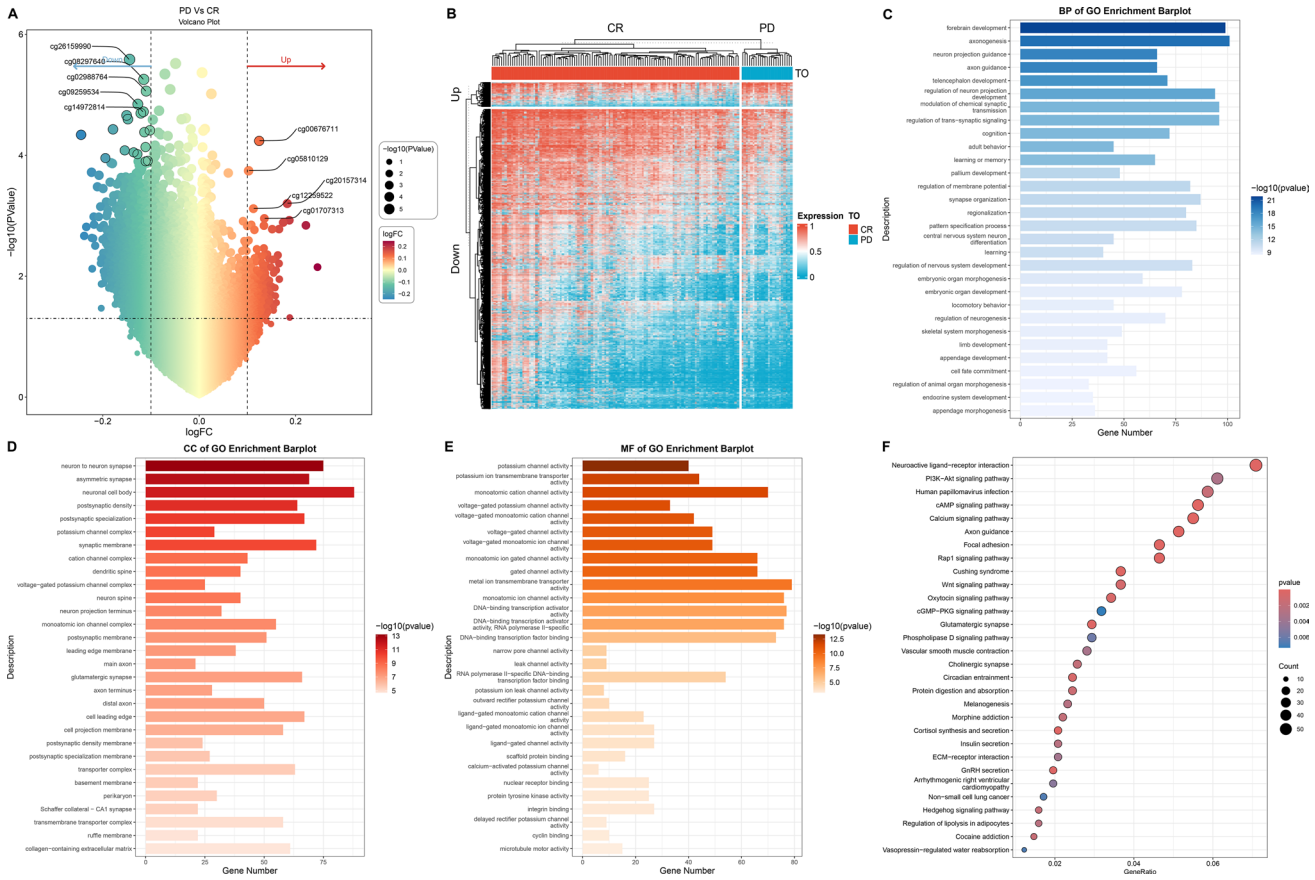

Fig. 2 Methylation difference analysis and enrichment analysis between radiotherapy-sensitive and insensitive groups. **A** Methylation difference analysis volcano plot, PD vs CR, the redder the marker the greater the up-regulation and the bluer the marker the greater the degree of down-regulation. **B** Methylation difference analysis heat map. **C** GO enrichment analysis The BP part enriched the most significant 30 entries, and the darker the colour, the more significant. **D** GO enrichment analysis The CC part enriched the most significant 30 articles, and the darker the colour, the more significant. **E** GO enrichment analysis of MF fraction results, the darker the colour the more significant. **F** KEGG enrichment analysis of the 30 most significant results

damage repair. Calcium signaling pathway: Calcium signaling pathway is involved in many cellular processes, such as cell proliferation, apoptosis and DNA repair. Abnormal activation of this pathway is associated with tumour formation and radiotherapy tolerance, and therefore may play an important role in tumour sensitivity to radiotherapy; Wnt signaling pathway, etc. (Fig. 2F).

3.3 Single-cell clustering downscaling and cellular annotation

After strict quality control, we finally obtained 43,475 cells. As can be seen from Fig. S1A, uniform manifold approximation and projection (UMI) and the amount of mRNA were significantly correlated, while the amount of UMI/mRNA was not significantly correlated with the content of mitochondrial genes. Figure 1B, C are the violin plots before and after the quality control (Fig. S1D). The results show that the batch effect between samples is very clearly eliminated.

Figure 3A shows the UMAP plot of the distribution of tumour samples and normal samples, Fig. 3B shows the UMAP plot of the distribution of aneuploid cells predicted by copykat, and Fig. 3C shows the UMAP plot of the distribution of subpopulations after annotation. A total of 13 types of cells were identified, namely pDC, B cells, DC, Plasma cells, Mast cells, Monocytes, ILC, Macro phages, Endothelial cells, Epithelial cells, Fibroblasts, T cells, and 9085 aneuploid cells were identified. In addition, we identified a total of 9085 aneuploid cells, which were concentrated in Epithelial cells, which is consistent with the origin of cervical cancer, and we also show the proportion of aneuploid cells in different cell types in each sample, with aneuploid cells only present in tumour samples (Fig. 3D). We identified 13 types of cells, including malignant cells, by cluster marker.

Here we show only the top 3 marker genes with the most prominent contributions expressed in each subgroup (Fig. 3E). Further, we analysed the pathways into which these 13 subpopulation differential genes were enriched (Fig. 3F).

3.4 Cell scoring

We intersected the differential genes with the genes involved in the differentially methylated sites and obtained 156 intersected genes (Fig. 4A). Then we scored the cells based on this set of genes and found that the cells with high scores were scattered in all types of cells, and the cells with the highest scores were located in Monocytes, ILCs, T cells and so on, and the scores in the same cell type showed a regional distribution (Fig. 4B). In the single-cell dataset, we performed AUCELL scoring for 156 genes and used an AUC threshold of > 0.031 to classify cells into high and low scoring groups. Subsequently, we conducted differential analysis between the high and low scoring cells. The GO enrichment analysis of differential genes significantly enriched keratinocyte differentiation, negative regulate of proteolysis, granulocyte migration in the BP fraction (Fig. 4E), and cytoplasmic vesicle lumen, complex of cytoplasmic vesicles, and cytoplasmic vesicle lumen in the CC fraction (Fig. 4C). The CC fraction was significantly enriched in cytoplasmic vesicle lumen, complex of collagen trimers, cortical cytoskeleton, etc. (Fig. 4F), and the MF fraction was significantly enriched in IgG binding, insulin-like growth factor binding, chemokine receptor binding, etc. (Fig. 4F). receptor binding, etc. (Fig. 4G). For the KEGG enrichment analysis, we found that the MF fraction was enriched in p53 signaling pathway, Focal adhesion, NF-kappa B signaling pathway, Leukocyte transendothelial migration, etc., which was more than what we had found in the previous bulk sequencing and methylation sequencing analyses. This echoed our previous results in batch sequencing and methylation sequencing (Fig. 4H).

3.5 Trajectory analysis

We first raised the malignant cells individually for trajectory analysis, by which we classified the malignant cells into 5 stages (Fig. 5A). We then identified the developmental starting point at State3 based on CytoTRACE and differentiated along State3 towards both ends (Fig. 5B, C). At the same time we also projected AUCell scores onto the cell developmental trajectories, and we found that relative to their stages, State4, state5 stages were distributed with more highly scored cells (Fig. 5D). Finally, we also analysed the enrichment of differential genes for each trajectory stage and found that State3 was enriched for Proteasome, P53 signaling pathway; State2 was enriched for Antigen processing and presentation, *Staphylococcus aureus* infection, Estrogen and P53 signaling pathway; State4 was enriched for P53 signaling pathway; and State5 was enriched for P53 signaling pathway. State2 was enriched in antigen processing and presentation, Staphylococcus aureus infection, estrogen signaling pathway, and State5 was enriched in oxidative phosphorylation.

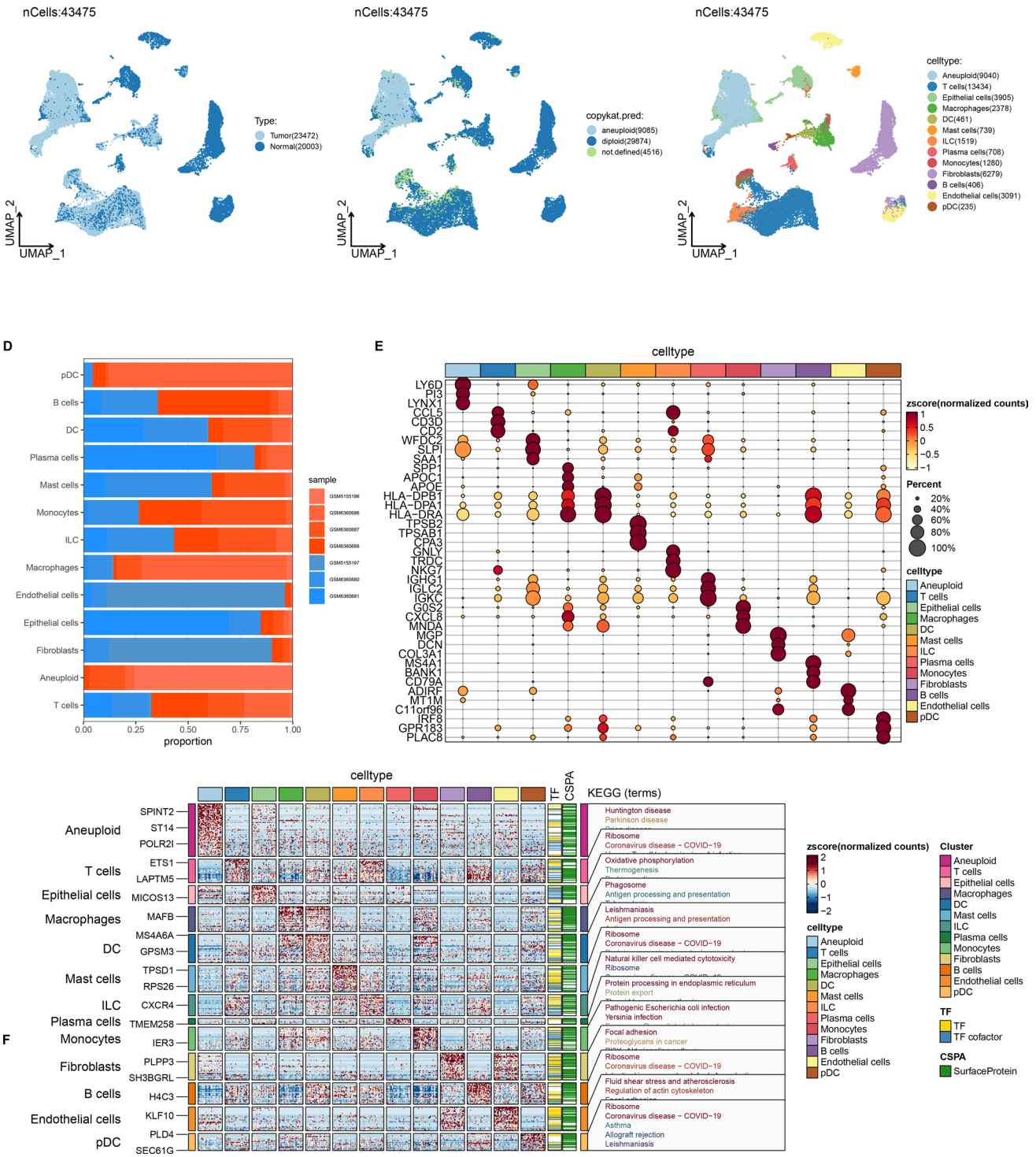

Fig. 3 Single-cell downscaling with cell type annotation. **A** UMAP plot of the distribution of tumour samples versus normal samples. **B** Results of the kopykat algorithm for identifying malignant cells. **C** UMAP plot of subpopulations after cell annotation. **D** the percentage of the sample in each type of cell, red is the cancer sample, blue is the normal sample. **E** The first three differences marker the various types of cells. **F** Heat map of differential marker enrichment for various cell types

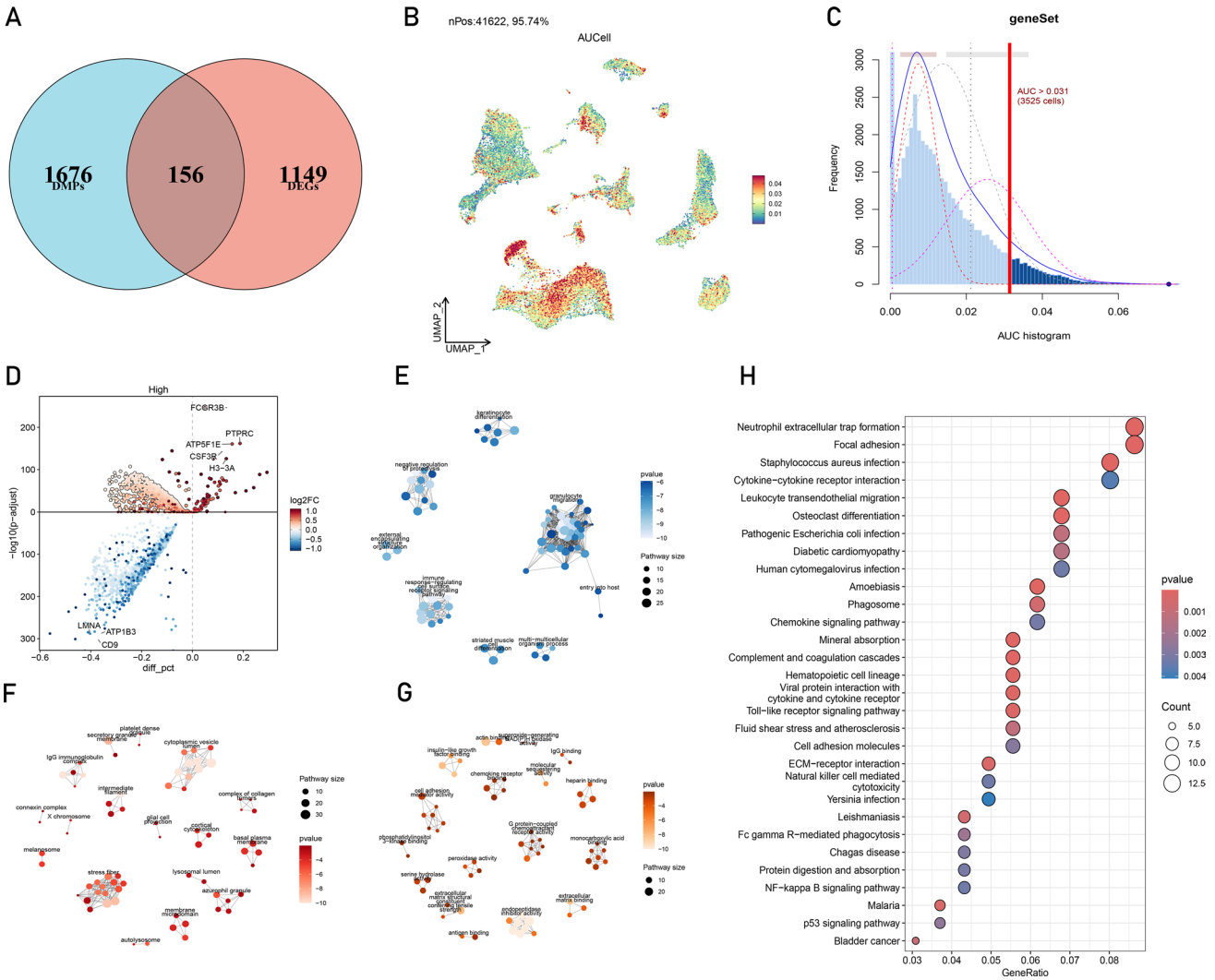

Fig. 4 Cell scoring based on genes related to radiotherapy sensitivity. **A** Differential genes and genes involved in differentially methylated loci intersecting genes. **B** UMAP distribution of AAUCell scores, with redder scores indicating higher scores. **C** AUC > 0.031 is used as a threshold to classify high and low scoring cells. **D** Differential analysis of high and low scoring cells, high scoring cells VS low scoring cells. **E** BP part of GO enrichment analysis of differential genes, the darker the colour, the more significant. **F** The CC part of the GO enrichment analysis of differential genes, the darker the colour, the more significant. **G** The MF part of the GO enrichment analysis of differential genes, the darker the colour, the more significant. **H** KEGG enrichment analysis of differential genes

These enrichment results suggested that cancer cells with relatively high sensitivity to radiotherapy might have some biological characteristics (Fig. 5E).

3.6 Machine learning to construct prognostic models

We performed a one-way Cox regression analysis of the genes intersecting the differential genes with the genes involved in the differentially methylated loci to obtain 6 Protective genes and 16 Risk genes (Fig. 6A). We then performed Lasso regression analysis and screened 10 genes. Based on these 10 genes (Fig. 6B), different algorithms were used to construct the model, and the results showed that the Cox model (Fig. 6C) and CoxBoost algorithm (Fig. 6D) performed the best,

Fig. 5 Trajectory analysis of malignant cells. **A** Trajectory analysis classified malignant cells into 5 developmental stages. **B** Proposed time of ▶ trajectory analysis, the redder the cell is at the end of development. **C** Developmental potential of cells predicted by CytoTRACE, the more erythrocytic the developmental potential, the less differentiated the malignant cells. **D** Distribution of ACUell scores over developmental trajectories. **E** Heat maps and enrichment results of differential genes at various stages of differentiation

while the GBM algorithm (Fig. 6E) and Random Forest Survival Algorithm (Fig. 6F) performed very well in the training set but poorly in the validation set. In the end, we chose the Cox algorithm to build the model.

Risk Score = 2.3883 × KCNJ6 + 0.0797 × ADD2 + 0.6324 × RGS6 − 0.8338 × SCUBE1 + 0.4831 × ZMAT4 + 0.3094 × LRRN4 + 0.0969 × SLC18 A3 − 0.1156 × CD7 − 0.2385 × JAKMIP1—0.4978 × CYP26 A1.

3.7 Comparison of models to clinical information

To examine the relationship between RiskScore scores and tumour clinical characteristics, we analysed the differences in RiskScore scores between clinical phenotypes in the TCGA dataset. The results showed that only the treatment outcome differed between the high- and low-risk groups, and there was no relationship with tumour stage, age, etc., suggesting that our radiotherapy-associated risk scores were independent of other tumour characteristics (Fig. 7A). To further illustrate the importance of the RiskScore, we chose to compare the age, T,N stage with the RiskScore in different prognostic perspectives of OS (Fig. 7B), DSS (Fig. 7C), DFI (Fig. 7D), PFI (Fig. 7E), and showed that the RiskScore had good performance in the four prognostic perspectives, both in the uni-factorial results and in the multi-factorial results. The results show that RiskScore has good performance in all four prognostic perspectives, both in single-factor and multi-factor results.

3.8 Immune infiltration

We identified a number of immune-related pathways in our enrichment results for bulk sequencing, so we also calculated the correlation of the risk score with the model genes and individual algorithmic immune scores (Fig. 8A), and found that the RiskScore was mainly negatively correlated with a number of important immune cells, such as the T cells MCPcounter, CD8 T.

cells xCel, ImmuneScore xCell, CD8 Tcm xCell, T cells CD8 CIBERSORT, etc. This result echoes our results in single cell scoring that highly scored cells are scattered among immune cells such as T cells (Fig. 8B). It is also interesting to note that the SCUB E1, CD7, and JAKMIP1 genes are positively correlated with many important immune cells in the model. We also visualised the scores of each algorithm in the same heatmap to depict the immune landscape between the highland groups of their risk scores (Fig. 8B).There are significant differences in immune infiltration between the high-risk and low-risk groups, specifically reflected in the markedly different abundances or scores of various immune cell subpopulations and microenvironment scores between the two groups(Fig. 8C). These differences may be closely related to disease progression, patient prognosis, and response to immunotherapy. By integrating multiple immune evaluation algorithms, we comprehensively revealed the complex associations between risk scores and the characteristics of the immune microenvironment.

3.9 Drug screening

We screened 3 drug candidates in CTRP which were TGX-221, DNMDP, NSC30930, CAL-101 (Fig. 9A). We screened 3 drug candidates in PRISM as lerisetron, t emocapril, ICI-162846 (Fig. 9B).

3.10 Expression of five genes and lerisetron functional analysis in radiotherapy resistance cervical cancer

KCNJ6, RGS6, SCUBE1, LRRN4, and JAKMIP1 are five newly identified genes associated with radiotherapy resistance in cervical cancer. Quantitative PCR (qPCR) (Fig. 10A–E) and immunohistochemistry analyses (Fig. 10F) demonstrated that

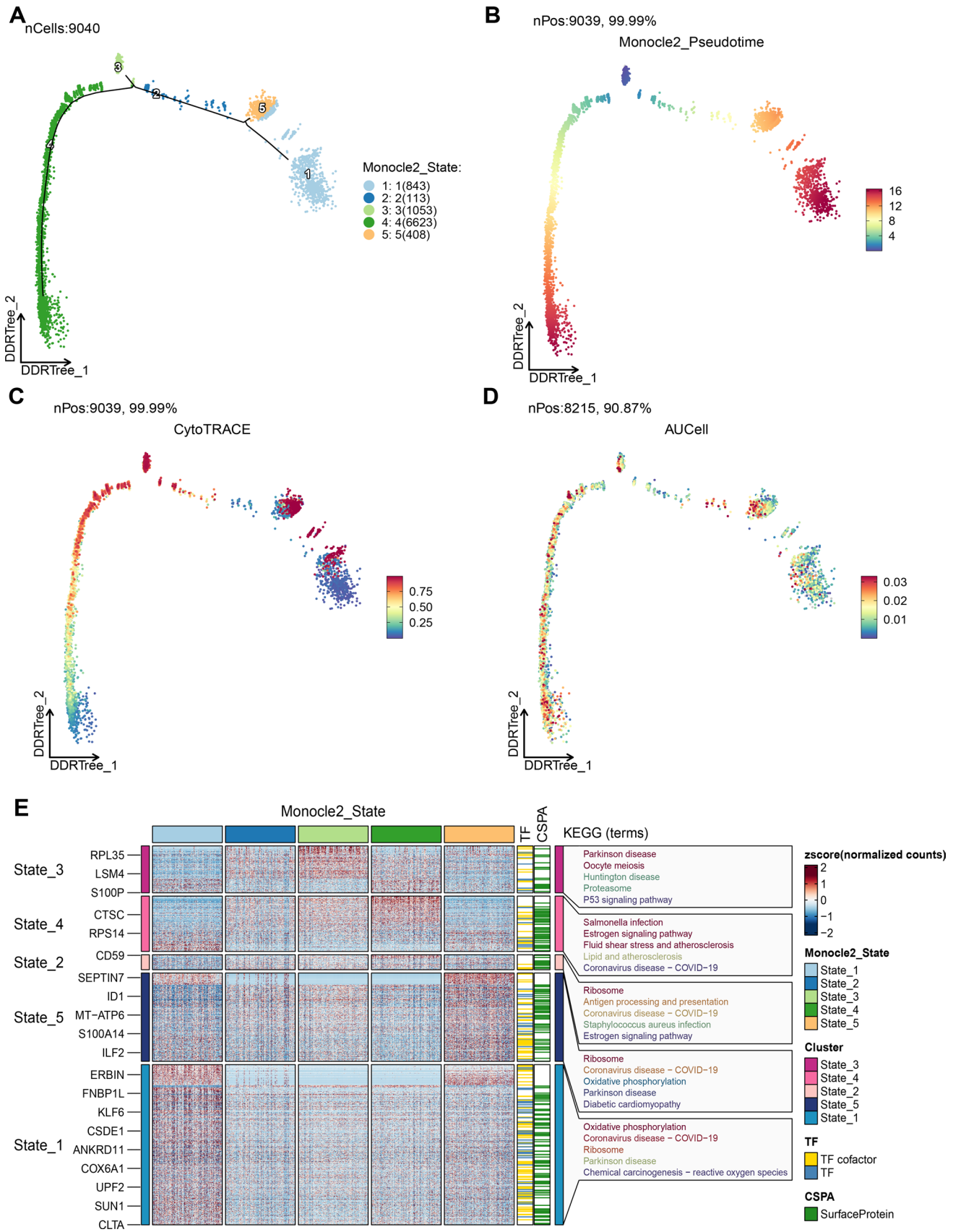
A
nCells:9040
Monocle2_State:
1: 1(843)
2: 2(113)
3: 3(1053)
4: 4(6623)
5: 5(408)
DDRTree_2
DDRTree_1
B
nPos:9039, 99.99%
Monocle2_Pseudotime
16
12
8
4
C
nPos:9039, 99.99%
CytoTRACE
0.75
0.50
0.25
D
nPos:8215, 90.87%
AUCell
0.03
0.02
0.01
E
Monocle2_State
TF
CSPA
KEGG (terms)
State_3
RPL35
LSM4
S100P
State_4
CTSC
RPS14
State_2
CD59
State_5
SEPTIN7
ID1
MT-ATP6
S100A14
ILF2
State_1
ERBIN
FNBP1L
KLF6
CSDE1
ANKRD11
COX6A1
UPF2
SUN1
CLTA
Parkinson disease
Oocyte meiosis
Huntington disease
Proteasome
P53 signaling pathway
Salmonella infection
Estrogen signaling pathway
Fluid shear stress and atherosclerosis
Lipid and atherosclerosis
Coronavirus disease - COVID-19
Ribosome
Antigen processing and presentation
Coronavirus disease - COVID-19
Staphylococcus aureus infection
Estrogen signaling pathway
Ribosome
Coronavirus disease - COVID-19
Oxidative phosphorylation
Parkinson disease
Diabetic cardiomyopathy
Oxidative phosphorylation
Coronavirus disease - COVID-19
Ribosome
Parkinson disease
Chemical carcinogenesis - reactive oxygen species
zscore(normalized counts)
2
1
0
−1
−2
Monocle2_State
State_1
State_2
State_3
State_4
State_5
Cluster
State_3
State_4
State_2
State_5
State_1
TF
TF cofactor
TF
CSPA
SurfaceProtein

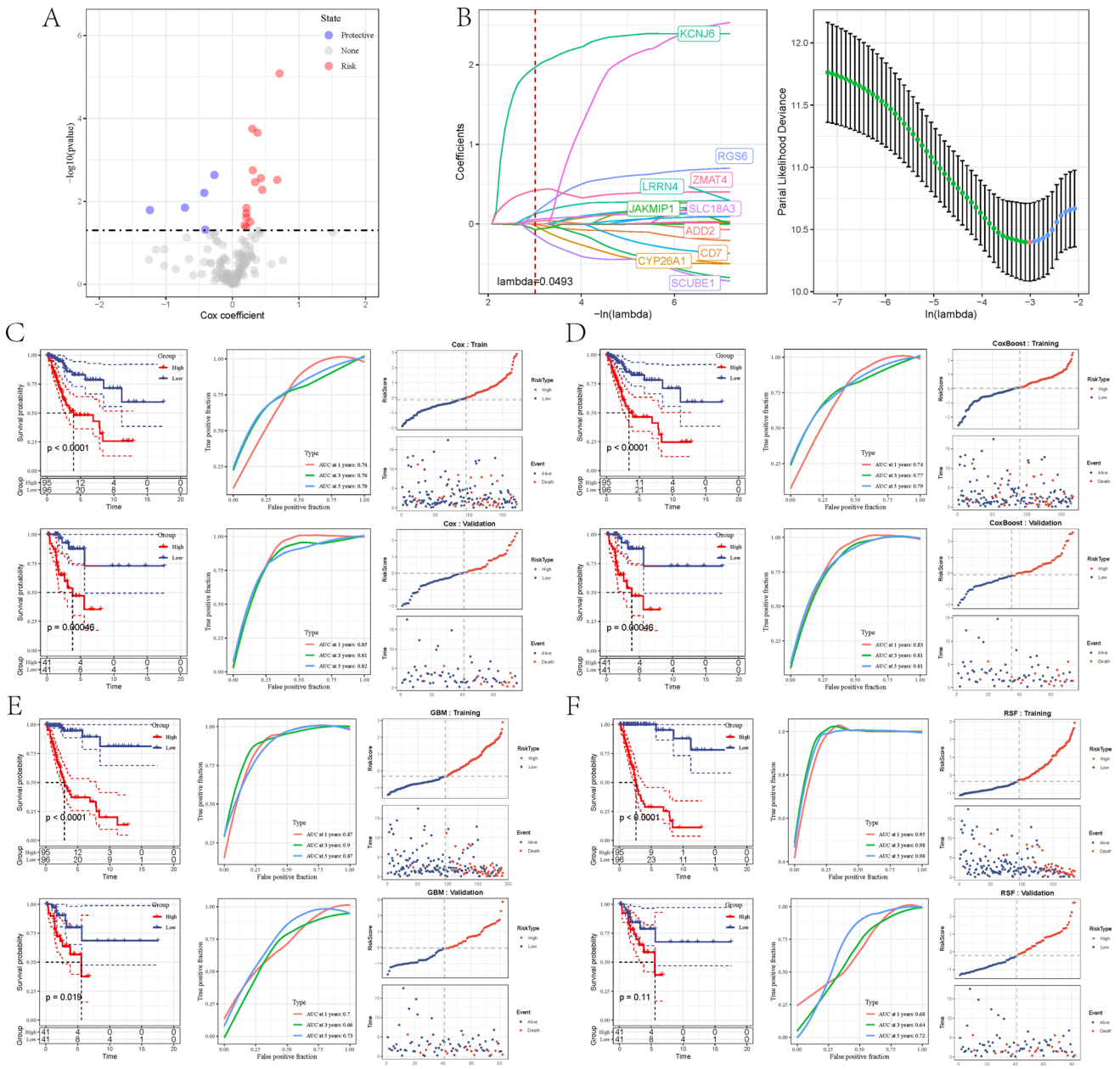

Fig. 6 Machine learning to construct prognostic models. **A** One-way Cox results for genes intersecting with genes involved in differentially methylated loci, with Risk genes in red and Protective genes in blue. **B** Lasso regression analysis for feature screening. **C** The Cox algorithm builds the prognostic model. The top shows the KM curve, ROC curve and Risk Score Distribution Plot of Cox in the training set, and the bottom shows the KM curve, ROC curve and Risk Score Distribution Plot of the training set. **D** The CoxBoost algorithm builds the prognostic model. The top shows the KM curve, ROC curve and Risk Score Distribution Plot of CoxBoost in the training set, and the bottom shows the KM curve, ROC curve and Risk Score Distribution Plot of the training set. **E** The GBM algorithm establishes the prognostic model. Above is the KM curve, ROC curve and Risk Score Distribution Plot of GBM in the training set, and below is the KM curve, ROC curve and Risk Score Distribution Plot of the training set. **F** The Random Forest Survival Algorithm builds a prognostic model, the top shows the KM curve, ROC curve and Risk Score Distribution Plot of the Random Forest Survival Algorithm in the training set, and the bottom shows the KM curve, ROC curve and Risk Score Distribution Plot of the training set

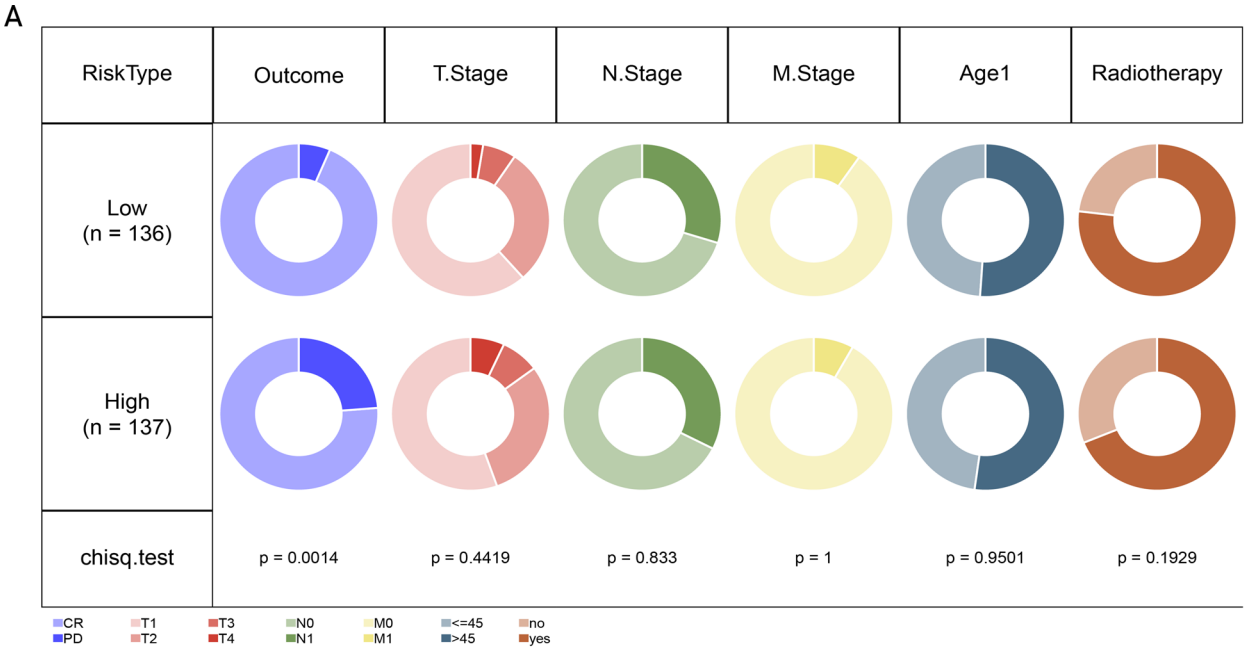

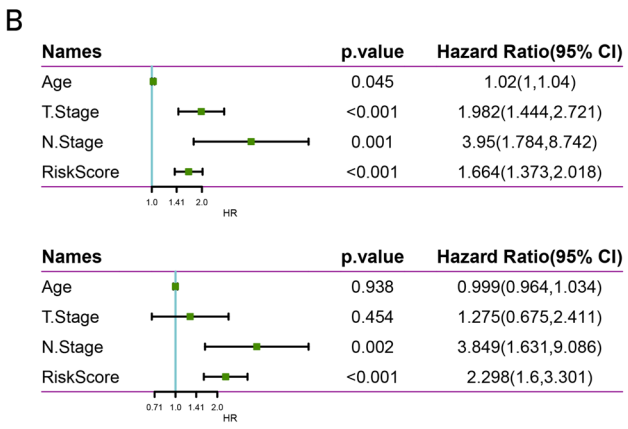

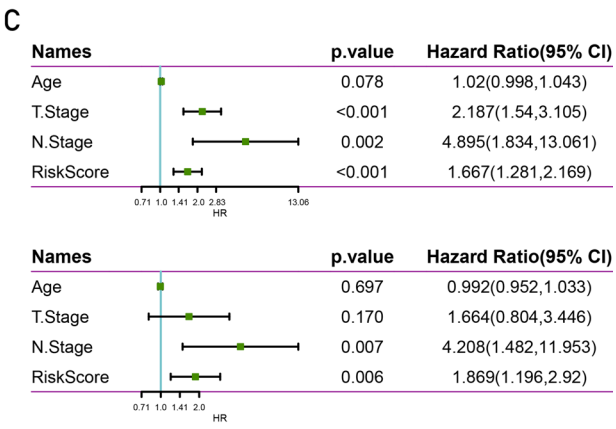

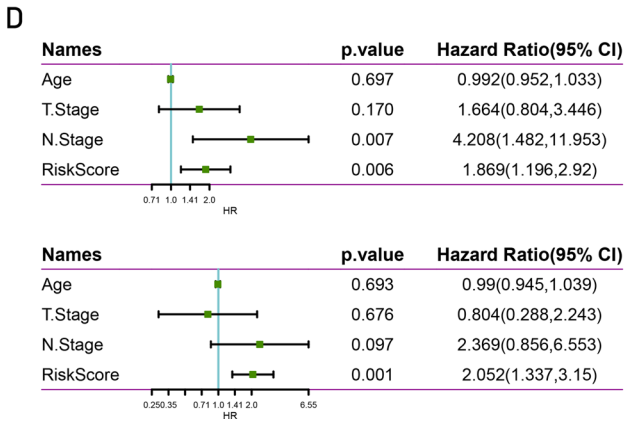

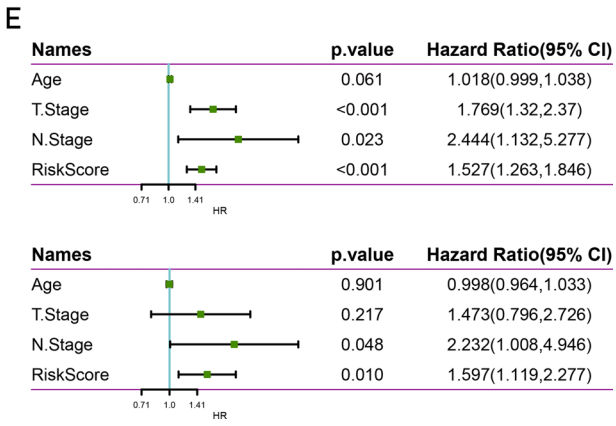

Fig. 7 Comparison of model scores with clinical information. **A** Comparison of clinical phenotypes between high and low score groups. **B** Age, T,N staging, RiskScore One-way Cox analysis at the OS level vs. multifactorial Cox analyses, with single factors above and multiple factors below. **C** Age, T, N staging, RiskScore One-way Cox analysis at the DSS level vs. multifactorial Cox Analyses, single factor above and multi-factor below. **D** Age, T,N staging, RiskScore One-way Cox analysis at the DFI level vs. multifactorial Cox Analyses, single factor above and multi-factor below. **E** Age, T, N staging, RiskScore One-way Cox analysis at the PFI level vs. multifactorial Cox Analyses, single factor above and multi-factor below

Fig. 8 Landscape of immune cell infiltration. **A** RiskScore and the correlation of model genes with each type of score. **B** Scatterplot of the correlation between RiskScore and some of the higher scoring cells. **C** MCPcounter, EPIC, xCell, CIBERSORT, quanTIseq, ESTIMATE, TIMER, and heatmap of 7 immunoassessment algorithms

the expression levels of KCNJ6, RGS6, and LRRN4 were significantly elevated in radiotherapy-resistant cervical cancer tissues compared to their expression in radiotherapy-sensitive tissues. Conversely, the expression of SCUBE1 and JAKMIP1 was notably decreased in radiotherapy-resistant cervical cancer tissues. In addition, we utilized information from the GTEx database to compare the expression levels of these five genes in normal cervical tissue and lesions to help validate our results (Figure S2).

Further, we explored the effect of Lerisentron on radiotherapy resistance of cervical cancer cells. A clone assay revealed that Lerisentron could effectively reverse the proliferative capacity of radiotherapy-resistant cervical cancer cells (Fig. 11A, B). Additionally, a Transwell assay indicated that Lerisentron could significantly inhibit the invasion and migration of these radiotherapy-resistant cancer cells (Fig. 11C, D). These findings suggest that these genes play a crucial role in mediating radiotherapy resistance and targeting them could provide a therapeutic strategy for overcoming resistance in cervical cancer treatment.

4 Discussion

Cervical cancer is one of the most common malignant tumors in women worldwide, with particularly high incidence in developing countries. Radiotherapy (RT) is a key treatment, but resistance to RT in some patients often leads to treatment failure [41]. Identifying therapeutic targets for RT resistance is therefore crucial.

This study investigated RT sensitivity mechanisms in cervical cancer using multi-omics and machine learning. Transcriptome analysis of TCGA samples identified 845 up-regulated and 460 down-regulated genes. GO analysis linked these genes to neuropeptide signaling, keratin formation, and hormone metabolism, while KEGG analysis highlighted neuroactive ligand-receptor interactions, cytokine-cytokine receptor interactions, and calcium signaling pathways. Differential methylation analysis revealed 3042 down-regulated and 158 up-regulated sites, associated with forebrain development, axonogenesis, and neural projection guidance. KEGG analysis pointed to roles for the cAMP, calcium, and Wnt signaling pathways in RT resistance. Single-cell analysis of 43,475 cells across 13 types showed that monocytes, ILCs, and T cells were most associated with RT sensitivity.

A prognostic model based on 10 key genes was constructed and validated, demonstrating strong predictive performance. Drug screening identified TGX-221, DNMDP, and CAL-101 as potential therapies for high-risk patients. Further experiments confirmed elevated KCNJ6, RGS6, and LRRN4, and reduced SCUBE1 and JAKMIP1, in RT-resistant tissues. Functional studies showed Lerisentron could reverse RT resistance.

Previous studies have shown that the KCNJ6 gene affects cell proliferation and apoptosis by regulating potassium channel activity [42]. In breast cancer, KCNJ6 has been found to promote tumor cell growth by increasing intracellular potassium ion concentration, but has been less well studied in cervical cancer [43]. In neuroblastoma, high expression of RGS6 is associated with G protein signaling inhibition and good prognosis, but the specific function in cervical cancer needs further study [44]. Serum levels of SCUBE1 in several cancers correlate with disease progression. In ovarian cancer, high expression of SCUBE1 correlates with tumor invasion and metastasis, but it has been less studied in cervical cancer [45]. In hepatocellular carcinoma, high expression of JAKMIP1 was correlated with tumour cell invasiveness, but was less studied in cervical cancer [46].

Further investigation revealed that these genes with known pathways related to RT resistance, such as Wnt signaling pathways, which play crucial roles in cervical cancer progression. Previous studies have demonstrated that the Wnt/β-catenin pathway is frequently activated in cervical cancer and contributes to tumor growth, glycolysis, and migration [47]. FAM83 F [48], PRAME, and DAX1 are examples of genes that promote cervical cancer progression by activating Wnt/β-catenin signaling, while HOXB4 inhibits tumorigenesis by repressing this pathway [49, 50]. These findings suggest that the genes identified in our study may similarly regulate RT resistance through modulation of these pathways, warranting further validation.

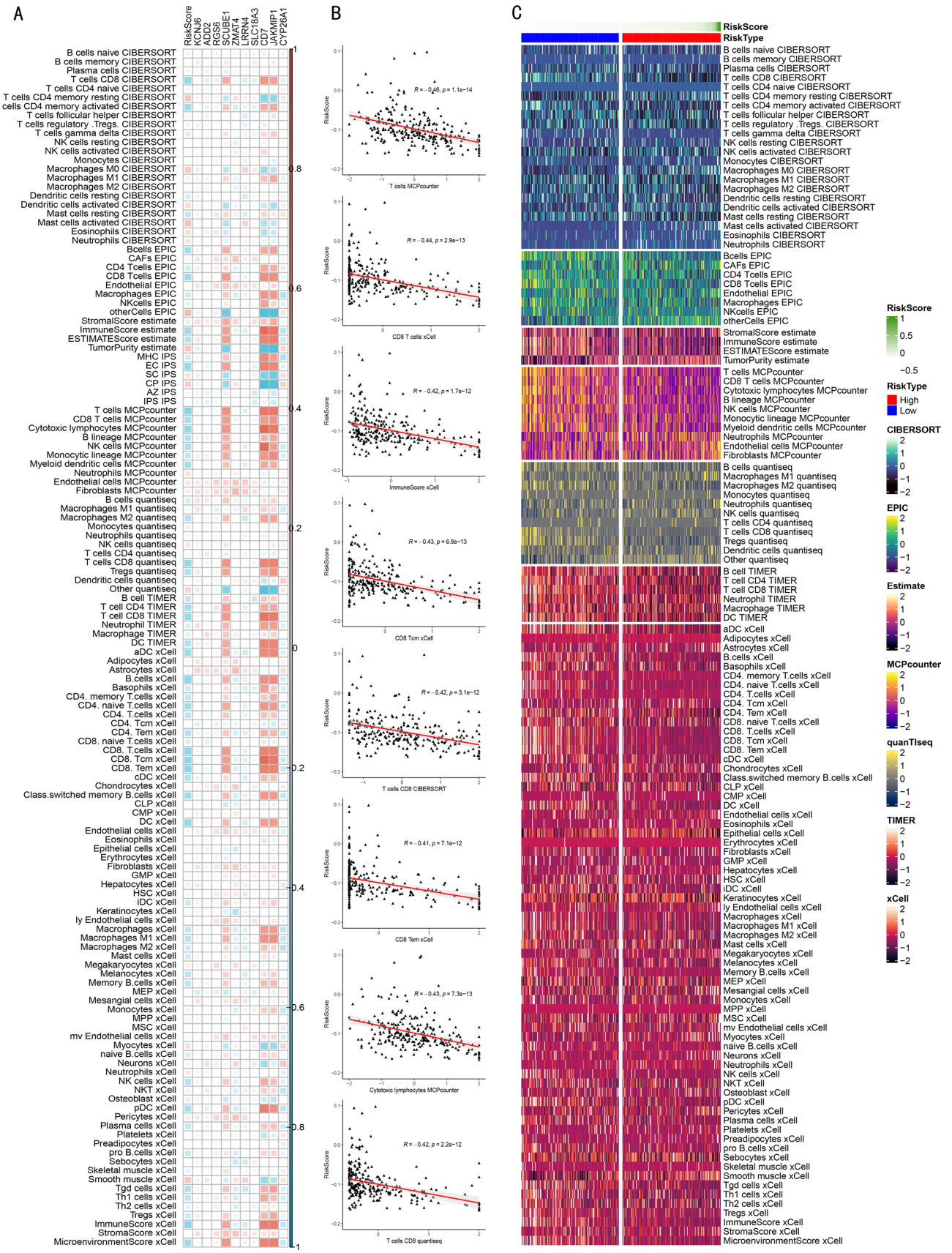
A
RiskScore
KCNJ6
ADD2
RGS6
SCUBE1
ZMAT4
LRRN4
SLC16A3
CD7
JAKMIP1
CYP26A1
B cells naive CIBERSORT
B cells memory CIBERSORT
Plasma cells CIBERSORT
T cells CD8 CIBERSORT
T cells CD4 naive CIBERSORT
T cells CD4 memory resting CIBERSORT
T cells CD4 memory activated CIBERSORT
T cells follicular helper CIBERSORT
T cells regulatory .Tregs. CIBERSORT
T cells gamma delta CIBERSORT
NK cells resting CIBERSORT
NK cells activated CIBERSORT
Monocytes CIBERSORT
Macrophages M0 CIBERSORT
Macrophages M1 CIBERSORT
Macrophages M2 CIBERSORT
Dendritic cells resting CIBERSORT
Dendritic cells activated CIBERSORT
Mast cells resting CIBERSORT
Mast cells activated CIBERSORT
Eosinophils CIBERSORT
Neutrophils CIBERSORT
Bcells EPIC
CAFs EPIC
CD4 Tcells EPIC
CD8 Tcells EPIC
Endothelial EPIC
Macrophages EPIC
NKcells EPIC
otherCells EPIC
StromalScore estimate
ImmuneScore estimate
ESTIMATEScore estimate
TumorPurity estimate
MHC IPS
EC IPS
SC IPS
CP IPS
AZ IPS
IPS IPS
T cells MCPcounter
CD8 T cells MCPcounter
Cytotoxic lymphocytes MCPcounter
B lineage MCPcounter
NK cells MCPcounter
Monocytic lineage MCPcounter
Myeloid dendritic cells MCPcounter
Neutrophils MCPcounter
Endothelial cells MCPcounter
Fibroblasts MCPcounter
B cells quantiseq
Macrophages M1 quantiseq
Macrophages M2 quantiseq
Monocytes quantiseq
Neutrophils quantiseq
NK cells quantiseq
T cells CD4 quantiseq
T cells CD8 quantiseq
Tregs quantiseq
Dendritic cells quantiseq
Other quantiseq
B cell TIMER
T cell CD4 TIMER
T cell CD8 TIMER
Neutrophil TIMER
Macrophage TIMER
DC TIMER
aDC xCell
Adipocytes xCell
Astrocytes xCell
B.cells xCell
Basophils xCell
CD4. memory T.cells xCell
CD4. naive T.cells xCell
CD4. T.cells xCell
CD4. Tcm xCell
CD4. Tem xCell
CD8. naive T.cells xCell
CD8. T.cells xCell
CD8. Tcm xCell
CD8. Tem xCell
cDC xCell
Chondrocytes xCell
Class.switched memory B.cells xCell
CLP xCell
CMP xCell
DC xCell
Endothelial cells xCell
Eosinophils xCell
Epithelial cells xCell
Erythrocytes xCell
Fibroblasts xCell
GMP xCell
Hepatocytes xCell
HSC xCell
iDC xCell
Keratinocytes xCell
ly Endothelial cells xCell
Macrophages xCell
Macrophages M1 xCell
Macrophages M2 xCell
Mast cells xCell
Megakaryocytes xCell
Melanocytes xCell
Memory B.cells xCell
MEP xCell
Mesangial cells xCell
Monocytes xCell
MPP xCell
MSC xCell
mv Endothelial cells xCell
Myocytes xCell
naive B.cells xCell
Neurons xCell
Neutrophils xCell
NK cells xCell
NKT xCell
Osteoblast xCell
pDC xCell
Pericytes xCell
Plasma cells xCell
Platelets xCell
Preadipocytes xCell
pro B.cells xCell
Sebocytes xCell
Skeletal muscle xCell
Smooth muscle xCell
Tgd cells xCell
Th1 cells xCell
Th2 cells xCell
Tregs xCell
ImmuneScore xCell
StromaScore xCell
MicroenvironmentScore xCell
1
0.8
0.6
0.4
0.2
0
0.2
0.4
0.6
0.8
1
B
R = −0.46, p = 1.1e−14
T cells MCPcounter
R = −0.44, p = 2.9e−13
CD8 T cells xCell
R = −0.42, p = 1.7e−12
ImmuneScore xCell
R = −0.43, p = 6.8e−13
CD8 Tcm xCell
R = −0.42, p = 3.1e−12
T cells CD8 CIBERSORT
R = −0.41, p = 7.1e−12
CD8 Tem xCell
R = −0.43, p = 7.3e−13
Cytotoxic lymphocytes MCPcounter
R = −0.42, p = 2.2e−12
T cells CD8 quantiseq
RiskScore
C
RiskScore
RiskType
RiskScore
1
0.5
0
−0.5
RiskType
High
Low
CIBERSORT
EPIC
Estimate
MCPcounter
quanTIseq
TIMER
xCell

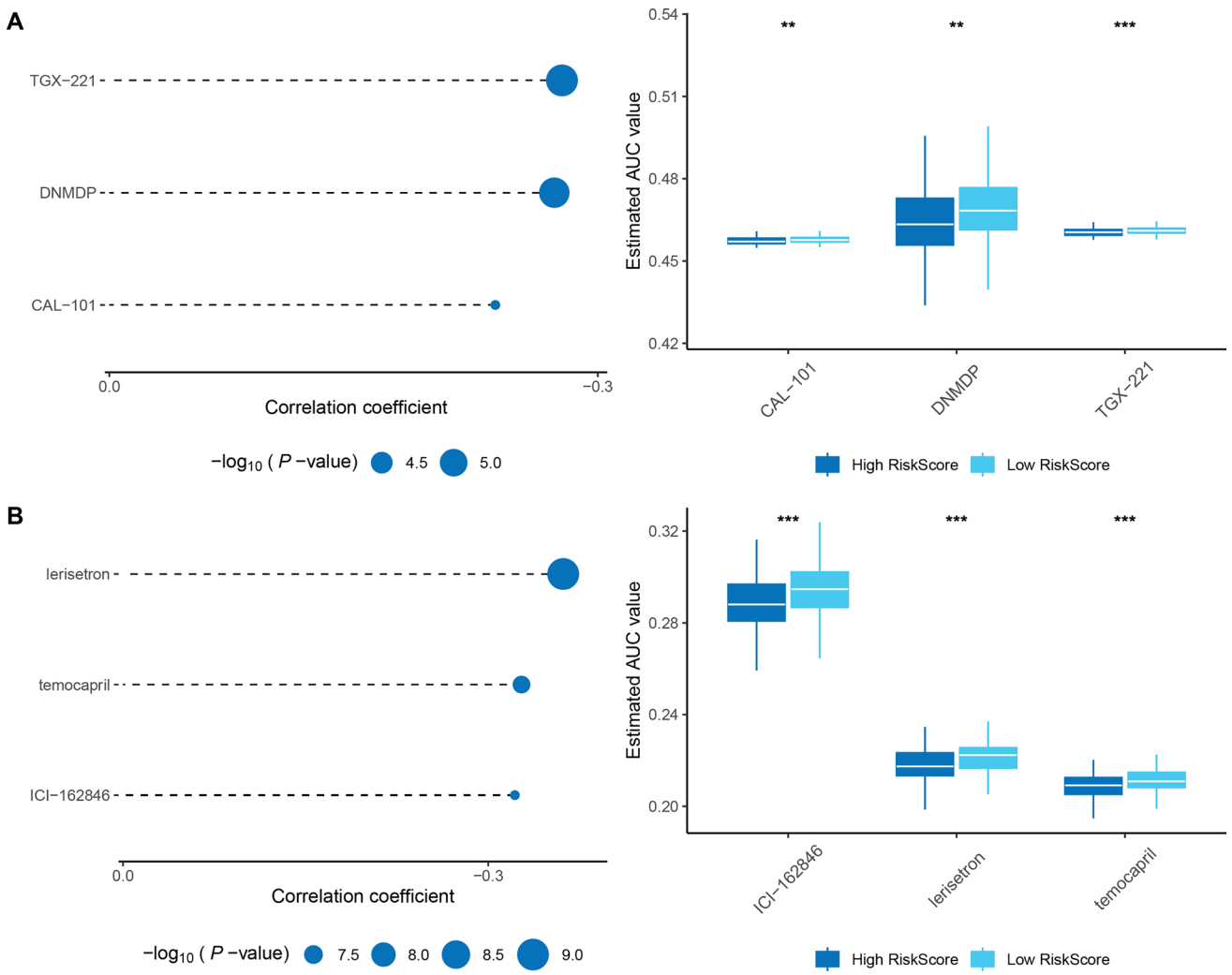

Fig. 9 Screening of drug candidates based on risk scores associated with radiosensitivity. **A** Drugs screened from the CTRP database, with correlations to RiskScore on the left and box plots of AUC in the upper and lower quartile samples of the RiskScore on the right. **B** Drugs screened from the PRISM database, with correlations with RiskScore on the left and box plots of AUC in the upper and lower quartile samples of the RiskScore on the right

Notably, LRRN4 has been implicated in tumor progression and poor prognosis in colon adenocarcinoma, where high LRRN4 expression was shown to link with WNT signaling pathway [51].

The potential therapeutic effects of Lerisentron in reversing RT resistance also deserve deeper exploration. Although studies on Lerisentron are limited, its role as a 5-HT2 A receptor antagonist may influence key signaling pathways, including Wnt/β-catenin [52]. The Wnt/β-catenin pathway has been widely implicated in RT resistance by promoting cell survival and DNA repair in cervical cancer [53]. Targeting this pathway has shown promise in enhancing RT efficacy [54]. We will focus on whether Lerisentron modulates these pathways directly or indirectly via the genes identified in our study, such as KCNJ6**,**RGS6 or LRRN4.

The above analysis revealed that KCNJ6, RGS6, SCUBE1, LRRN4, and JAKMIP1 genes are still less studied in cervical cancer, and in this study we confirmed that the expression of KCNJ6, RGS6, and LRRN4 was elevated in radiotherapy-resistant tissues of cervical cancer by qpcr and immunohistochemistry experiments, and that the expression of SCUBE1 and JAKMIP1 genes was elevated in the SCUBE1 and JAKMIP1 genes were decreased in radiotherapy-resistant tissues of cervical cancer, and these genes may provide new target genes for future studies.

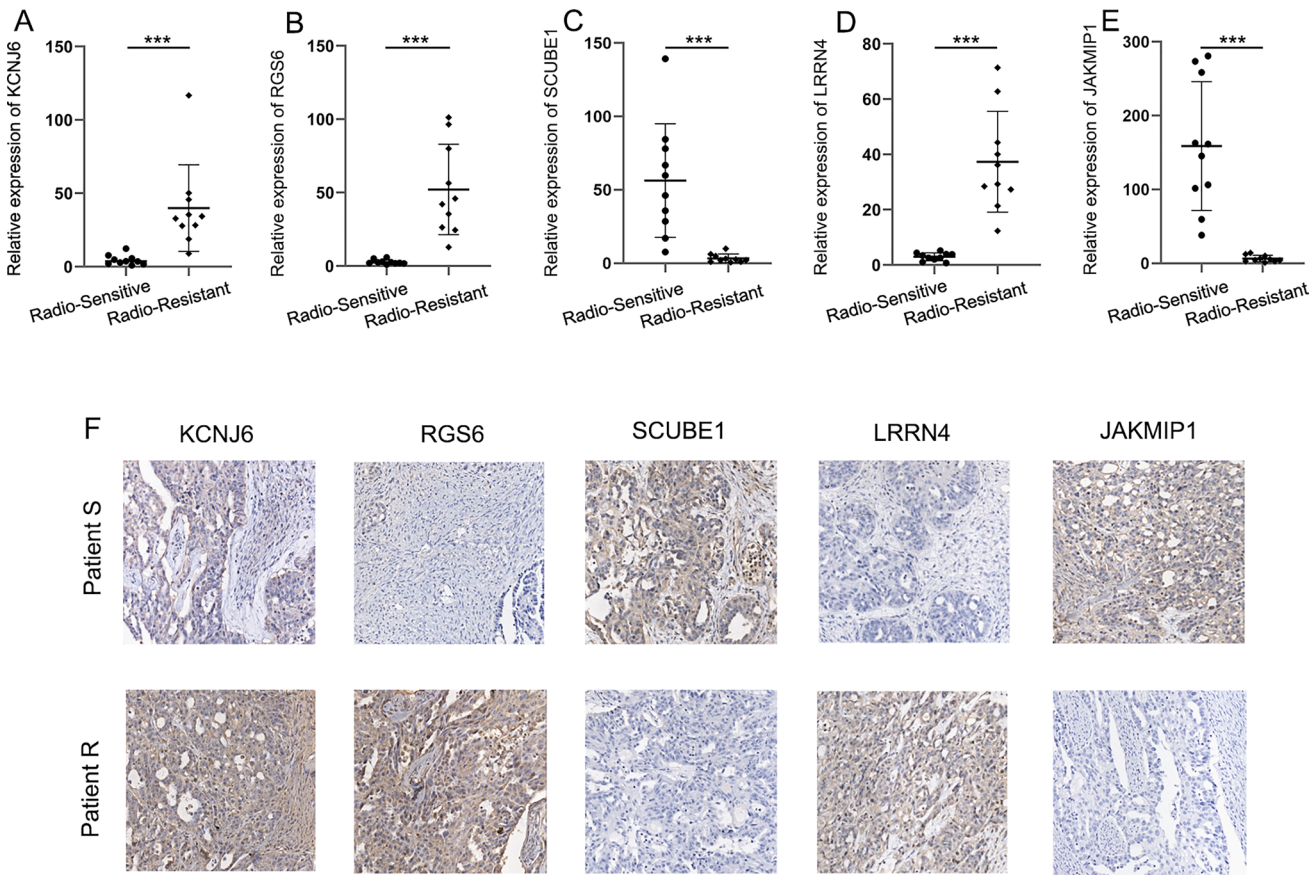

Fig. 10 Expression Analysis of Radiotherapy-Resistance-Associated Genes in Cervical Cancer Tissues. **A–E** Quantitative PCR (qPCR) analysis showing the elevated expression levels of KCNJ6, RGS6, and LRRN4 in radiotherapy-resistant cervical cancer tissues compared to radiotherapy-sensitive tissues. **F** Immunohistochemistry analysis depicting the differential expression of SCUBE1 and JAKMIP1, with decreased levels in radiotherapy-resistant tissues

5 Conclusion

In this study, we systematically explored the molecular mechanisms of radiotherapy sensitivity in cervical cancer by integrating multi-omics analyses and single-cell sequencing technologies. We identified multiple potential therapeutic targets and prognostic markers and constructed a robust prognostic model with strong predictive ability across multiple datasets. Additionally, we screened potential therapeutic agents with high sensitivity for high-risk patients. These findings provide a valuable reference for developing personalised therapeutic strategies for cervical cancer and hold promise for clinical applications. Future studies should focus on investigating the specific mechanisms of these markers and validating their clinical effectiveness to improve therapeutic outcomes and enhance survival rates for cervical cancer patients.

This study also has some shortcomings, as follows: this study utilised multi-omics data from TCGA and GEO databases, but the sample size is still limited; future studies should expand the sample size to improve the reliability of the results. Secondly, this paper is mainly based on bioinformatics analysis and lacks experimental validation; the functions of key genes and signalling pathways should be further verified by in vitro and in vivo experiments in the future. In terms of clinical application, although this study constructed a prognostic model, further validation and optimisation are needed in practical application.

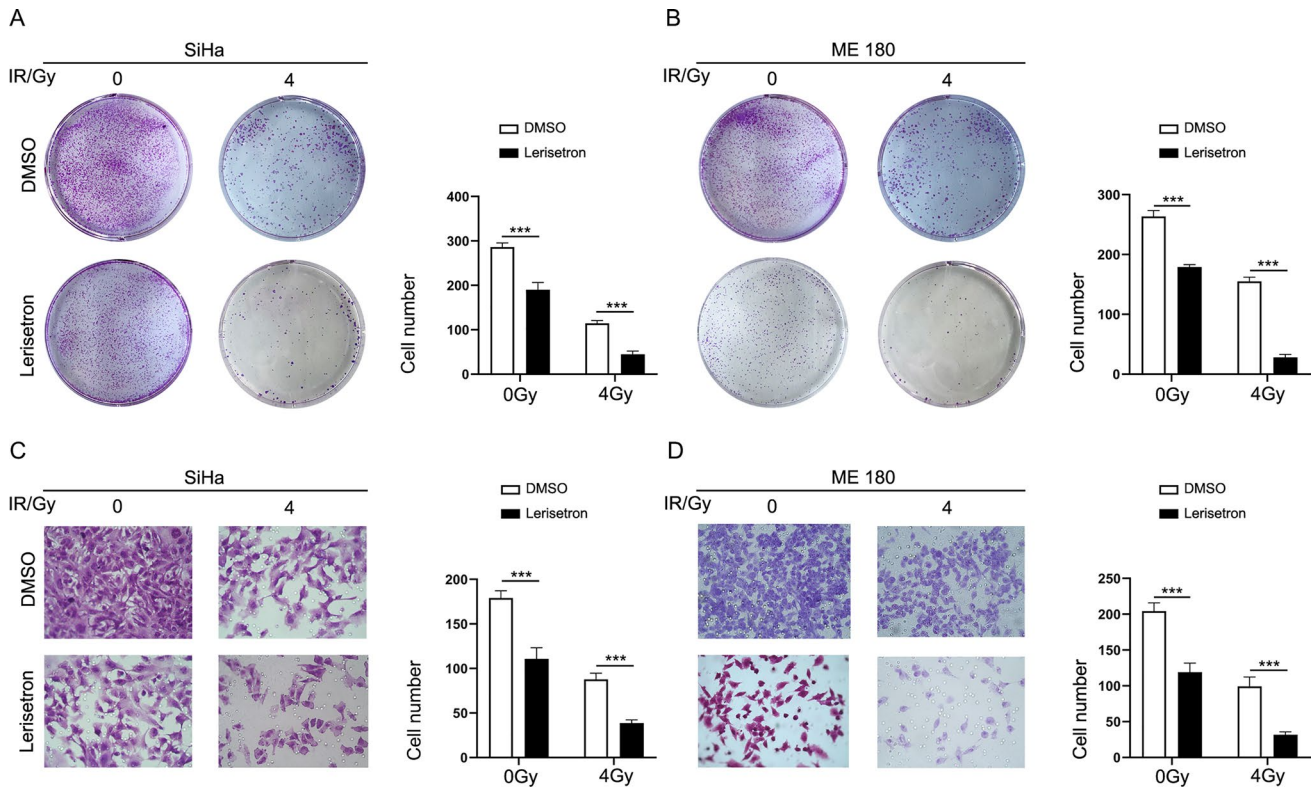

Fig. 11 Effects of lerisentron on radiotherapy-resistant cervical cancer cells. **A**, **B** Clonogenic assay results indicating that Lerisentron effectively reverses the proliferation capacity of radiotherapy-resistant cervical cancer cells. **C**, **D** Transwell assay demonstrating that Lerisentron significantly inhibits the invasion and migration capabilities of radiotherapy-resistant cervical cancer cells

Acknowledgements We would like to thank TCGA, GTEx and GEO databases for the availability of the data.

Author contributions Yang Liu: Conceptualization, Methodology, Investigation, Data curation, Writing—original draft Xin Pan: Methodology, Software, Formal analysis, Data curation Xu Zhang: Validation, Investigation, Data curation Bo Tan: Software, Formal analysis, Visualization Rui Ran: Investigation, Resources Li Liu: Investigation, Resources Lin Yang: Writing—review & editing, Supervision.

Funding Chongqing Natural Science Foundation General Program (cstc2021jcyj-msxmX0037).

Data availability The datasets used or analysed during the current study are available from the corresponding author on reasonable request.

Declarations

Ethics approval and consent to participate The study was approved by the Ethics Committee of The Second Affiliated Hospital of Chongqing Medical University Informed consent was obtained from all participants in the study. The study was performed in accordance with the ethical standards as laid down in the 1964 Declaration of Helsinki and its later amendments standards.

Consent for publication Not applicable.

Competing interests The authors declare no competing interests.

References

1. Cohen PA, Jhingran A, Oaknin A, Denny L. Cervical cancer. The Lancet. 2019;393(10167):169–82. https://doi.org/10.1016/S0140-6736(18)32470-X.
2. Arbyn M, et al. Estimates of incidence and mortality of cervical cancer in 2018: a worldwide analysis. Lancet Glob Health. 2020;8(2):e191–203. https://doi.org/10.1016/S2214-109X(19)30482-6.
3. Bray F, et al. Global cancer statistics 2022: GLOBOCAN estimates of incidence and mortality worldwide for 36 cancers in 185 countries. CA Cancer J Clin. 2024;74(3):229–63. https://doi.org/10.3322/caac.21834.
4. Yuan Y, Cai X, Shen F, Ma F. HPV post-infection microenvironment and cervical cancer. Cancer Lett. 2021;497:243–54. https://doi.org/10.1016/j.canlet.2020.10.034.
5. Bhatla N, Singhal S. Primary HPV screening for cervical cancer. Best Pract Res Clin Obstet Gynaecol. 2020;65:98–108. https://doi.org/10.1016/j.bpobgyn.2020.02.008.
6. Abu-Rusthum NR, et al. NCCN Guidelines® Insights: Cervical Cancer, Version 1.2024. J Natl Compr Canc Netw. 2023;21(12):1224–33. https://doi.org/10.6004/jnccn.2023.0062.
7. Li H, Wu X, Cheng X. Advances in diagnosis and treatment of metastatic cervical cancer. J Gynecol Oncol. 2016;27(4): e43. https://doi.org/10.3802/jgo.2016.27.e43.
8. Liontos M, Kyriazoglou A, Dimitriadis I, Dimopoulos M-A, Bamias A. Systemic therapy in cervical cancer: 30 years in review. Crit Rev Oncol Hematol. 2019;137:9–17. https://doi.org/10.1016/j.critrevonc.2019.02.009.
9. Ferrall L, Lin KY, Roden RBS, Hung C-F, Wu T-C. Cervical cancer immunotherapy: facts and hopes. Clin Cancer Res. 2021;27(18):4953–73. https://doi.org/10.1158/1078-0432.CCR-20-2833.
10. Hata M. Radiation therapy for elderly patients with uterine cervical cancer: feasibility of curative treatment. Int J Gynecol Cancer. 2019;29(3):622–9. https://doi.org/10.1136/ijgc-2018-000077.
11. Cho WK, Park W, Kim S-W, Lee KK, Ahn KJ, Choi JH. Postoperative hypofractionated intensity-modulated radiotherapy with concurrent chemotherapy in cervical cancer: The POHIM-CCRT nonrandomized controlled trial. JAMA Oncol. 2024;10(6):737. https://doi.org/10.1001/jamaoncol.2024.0565.
12. Feng Y, et al. Identification of biomarkers for cervical cancer radiotherapy resistance based on RNA sequencing data. Front Cell Dev Biol. 2021;9: 724172. https://doi.org/10.3389/fcell.2021.724172.
13. Tellez-Gabriel M, Ory B, Lamoureux F, Heymann M-F, Heymann D. Tumour heterogeneity: the key advantages of single-cell analysis. Int J Mol Sci. 2016;17(12):2142. https://doi.org/10.3390/ijms17122142.
14. Keller L, Pantel K. Unravelling tumour heterogeneity by single-cell profiling of circulating tumour cells. Nat Rev Cancer. 2019;19(10):553–67. https://doi.org/10.1038/s41568-019-0180-2.
15. Wei E, Reisinger A, Li J, French LE, Clanner-Engelshofen B, Reinholz M. Integration of scRNA-Seq and TCGA RNA-Seq to analyze the heterogeneity of HPV+ and HPV- cervical cancer immune cells and establish molecular risk models. Front Oncol. 2022;12: 860900. https://doi.org/10.3389/fonc.2022.860900.
16. Wu Y, Song Y, Wang R, Wang T. Molecular mechanisms of tumor resistance to radiotherapy. Mol Cancer. 2023;22(1):96. https://doi.org/10.1186/s12943-023-01801-2.
17. Chen X, et al. Analysis of DNA methylation and gene expression in radiation-resistant head and neck tumors. Epigenetics. 2015;10(6):545–61. https://doi.org/10.1080/15592294.2015.1048953.
18. Goldman MJ, et al. Visualizing and interpreting cancer genomics data via the Xena platform. Nat Biotechnol. 2020;38(6):675–8. https://doi.org/10.1038/s41587-020-0546-8.
19. Robinson MD, McCarthy DJ, Smyth GK. edgeR: a Bioconductor package for differential expression analysis of digital gene expression data. Bioinformatics. 2010;26(1):139–40. https://doi.org/10.1093/bioinformatics/btp616.
20. Morris TJ, et al. ChAMP: 450k chip analysis methylation pipeline. Bioinformatics. 2014;30(3):428–30. https://doi.org/10.1093/bioinformatics/btt684.
21. Hao Y, et al. Integrated analysis of multimodal single-cell data. Cell. 2021;184(13):3573-3587.e29. https://doi.org/10.1016/j.cell.2021.04.048.
22. Li C, Guo L, Li S, Hua K. Single-cell transcriptomics reveals the landscape of intra-tumoral heterogeneity and transcriptional activities of ECs in CC. Mol Ther Nucleic Acids. 2021;24:682–94. https://doi.org/10.1016/j.omtn.2021.03.017.
23. Guo C, et al. Spatiotemporally deciphering the mysterious mechanism of persistent HPV-induced malignant transition and immune remodelling from HPV-infected normal cervix, precancer to cervical cancer: Integrating single-cell RNA-sequencing and spatial transcriptome. Clin Transl Med. 2023;13(3): e1219. https://doi.org/10.1002/ctm2.1219.
24. Korsunsky I, et al. Fast, sensitive and accurate integration of single-cell data with Harmony. Nat Methods. 2019;16(12):1289–96. https://doi.org/10.1038/s41592-019-0619-0.
25. Domínguez Conde C, et al. Cross-tissue immune cell analysis reveals tissue-specific features in humans. Science. 2022;376(6594):eabl5197. https://doi.org/10.1126/science.abl5197.
26. Gao R, et al. Delineating copy number and clonal substructure in human tumors from single-cell transcriptomes. Nat Biotechnol. 2021;39(5):599–608. https://doi.org/10.1038/s41587-020-00795-2.
27. 'GitHub - zhanghao-njmu/SCP: An end-to-end Single-Cell Pipeline designed to facilitate comprehensive analysis and exploration of single-cell data.' Accessed: Feb. 19, 2025. [Online]. Available: https://github.com/zhanghao-njmu/SCP
28. Aibar S, et al. SCENIC: single-cell regulatory network inference and clustering. Nat Methods. 2017;14(11):1083–6. https://doi.org/10.1038/nmeth.4463.
29. Gulati GS, et al. Single-cell transcriptional diversity is a hallmark of developmental potential. Science. 2020;367(6476):405–11. https://doi.org/10.1126/science.aax0249.
30. Engebretsen S, Bohlin J. Statistical predictions with glmnet. Clin Epigenetics. 2019;11(1):123. https://doi.org/10.1186/s13148-019-0730-1.

31. Therneau TM, Grambsch PM. Modeling survival data: extending the Cox model. In: Statistics for biology and health. New York: Springer; 2000.
32. 'CoxBoost: Cox models by likelihood based boosting for a single survival endpoint or competing risks version 1.4 from CRAN'. Accessed: Feb. 19, 2025. [Online]. Available: https://rdrr.io/cran/CoxBoost/
33. G. Ridgeway *et al.*, *gbm: Generalized Boosted Regression Models*. (Jun. 28, 2024). Accessed: Feb. 19, 2025. [Online]. Available: https://cran.r-project.org/web/packages/gbm/index.html
34. 'randomForestSRC: Fast Unified Random Forests for Survival, Regression, and Classification (RF-SRC) version 3.3.1 from CRAN'. Accessed: Feb. 19, 2025. [Online]. Available: https://rdrr.io/cran/randomForestSRC/
35. Zeng D, et al. IOBR: multi-omics immuno-oncology biological research to decode tumor microenvironment and signatures. Front Immunol. 2021;12: 687975. https://doi.org/10.3389/fimmu.2021.687975.
36. Ghandi M, et al. Next-generation characterization of the cancer cell line Encyclopedia. Nature. 2019;569(7757):503–8. https://doi.org/10.1038/s41586-019-1186-3.
37. Geeleher P, Cox N, Huang RS. pRRophetic: an R package for prediction of clinical chemotherapeutic response from tumor gene expression levels. PLoS ONE. 2014;9(9): e107468. https://doi.org/10.1371/journal.pone.0107468.
38. Yang C, Huang X, Li Y, Chen J, Lv Y, Dai S. Prognosis and personalized treatment prediction in TP53-mutant hepatocellular carcinoma: an in silico strategy towards precision oncology. Brief Bioinform. 2021;22(3): bbaa164. https://doi.org/10.1093/bib/bbaa164.
39. Wu T, et al. clusterProfiler 4.0: A universal enrichment tool for interpreting omics data. Innovation (Camb). 2021;2(3): 100141. https://doi.org/10.1016/j.xinn.2021.100141.
40. Kerseviciute I, Gordevicius J. aPEAR: an R package for autonomous visualization of pathway enrichment networks. Bioinformatics. 2023;39(11): btad672. https://doi.org/10.1093/bioinformatics/btad672.
41. Zhang H, et al. Review of possible mechanisms of radiotherapy resistance in cervical cancer. Front Oncol. 2023;13: 1164985. https://doi.org/10.3389/fonc.2023.1164985.
42. Zhang W, Das P, Kelangi S, Bei M. Potassium channels as potential drug targets for limb wound repair and regeneration. Precis Clin Med. 2020;3(1):22–33. https://doi.org/10.1093/pcmedi/pbz029.
43. Liu J, Li C. Data-driven energy landscape reveals critical genes in cancer progression. NPJ Syst Biol Appl. 2024;10(1):1–11. https://doi.org/10.1038/s41540-024-00354-4.
44. Liu Z, Fisher RA. RGS6 interacts with DMAP1 and DNMT1 and inhibits DMAP1 transcriptional repressor activity. J Biol Chem. 2004;279(14):14120–8. https://doi.org/10.1074/jbc.M309547200.
45. Kumar S, Prajapati KS, Gupta S. The multifaceted role of signal peptide-CUB-EGF domain-containing protein (SCUBE) in cancer. Int J Mol Sci. 2022;23(18):10577. https://doi.org/10.3390/ijms231810577.
46. Gill PS, et al. Integrated microRNA-mRNA expression profiling identifies novel targets and networks associated with autism. J Pers Med. 2022;12(6):920. https://doi.org/10.3390/jpm12060920.
47. Yang M, et al. Wnt signaling in cervical cancer? J Cancer. 2018;9(7):1277–86. https://doi.org/10.7150/jca.22005.
48. Zhang C, et al. Upregulation of FAM83F by c-Myc promotes cervical cancer growth and aerobic glycolysis via Wnt/β-catenin signaling activation. Cell Death Dis. 2023;14(12):837. https://doi.org/10.1038/s41419-023-06377-9.
49. Lei D, Yang W-T, Zheng P-S. HOXB4 inhibits the proliferation and tumorigenesis of cervical cancer cells by downregulating the activity of Wnt/β-catenin signaling pathway. Cell Death Dis. 2021;12(1):105. https://doi.org/10.1038/s41419-021-03411-6.
50. Liu X-F, Li X-Y, Zheng P-S, Yang W-T. DAX1 promotes cervical cancer cell growth and tumorigenicity through activation of Wnt/β-catenin pathway via GSK3β. Cell Death Dis. 2018;9(3):339. https://doi.org/10.1038/s41419-018-0359-6.
51. Zhang Y, Xie J, Liu D, Zhu S, Zhang S. The expression of LRRN4 was correlated with the progression and prognosis of colon adenocarcinoma (COAD) patients. Genet Mol Biol. 2021;45(1): e20210138. https://doi.org/10.1590/1678-4685-GMB-2021-0138.
52. Fatima S, et al. 5-Hydroxytryptamine promotes hepatocellular carcinoma proliferation by influencing β-catenin. Mol Oncol. 2016;10(2):195–212. https://doi.org/10.1016/j.molonc.2015.09.008.
53. Zhang J, et al. Inhibition of Wnt signalling pathway by XAV939 enhances radiosensitivity in human cervical cancer HeLa cells. Artif Cells Nanomed Biotechnol. 2020;48(1):479–87. https://doi.org/10.1080/21691401.2020.1716779.
54. Wen R, et al. DSTN hypomethylation promotes radiotherapy resistance of rectal cancer by activating the Wnt/β-catenin signaling pathway. Int J Radiat Oncol Biol Phys. 2023;117(1):198–210. https://doi.org/10.1016/j.ijrobp.2023.03.067.